Local Energetics of Kinetic Energy Divided in the Barotropic and Baroclinic Components during the Formation of Blocking

Yasushi WATARAI

A dissertation submitted to
the Doctoral Program in Geoscience,
the University of Tsukuba
in partial fulfillment of the requirements
for the degree of Doctor of Philosophy in Science

February 2004

Local Energetics of Kinetic Energy Divided in the Barotropic and Baroclinic Components during the Formation of Blocking

Yasushi WATARAI

A dissertation submitted to
the Doctoral Program in Geoscience,
the University of Tsukuba
in partial fulfillment of the requirements
for the degree of Doctor of Philosophy in Science

February 2004

ABSTRACT

In this study, the characteristics of barotropic-baroclinic interactions, $C(K_s, K_m)$, for atmospheric blocking using the NCEP/NCAR dataset are firstly examined. Kinetic energy budget is then performed in the framework of the vertical mean and sheared flows, and the energetics terms including the barotropic-baroclinic interactions, $C(K_s, K_m)$, are analyzed.

As a result of composite analysis for the 10 typical blockings over Alaska, it is confirmed that there are two maxima of $C(K_s, K_m)$ located along the western and eastern flanks of the blocking ridge, indicating that the baroclinic kinetic energy is converted to the barotropic kinetic energy in those regions. These maxima are almost represented by the nondivergent part of the barotropic-baroclinic interactions, $C_{ND}(K_s, K_m)$, which is related to the temperature advection. In addition, the 10 thpical blockings over Europe show the same characteristics as that over Alaska.

Secondly, the local energetics analysis for the blocking formation at the North Pacific in threshold of a transient ridge to become a blocking is performed. Among the total number of 452 ridges, 88 are identified as blocking during 51 winters1950 to 2001.

As a result, it is found that a blocking becomes Ω type for large $C(K_s, K_m)$, and

it becomes dipole type for small $C(K_s, K_m)$. It is also shown for the large $C(K_s, K_m)$ that a ridge develops to a blocking when the flux convergence of mechanical energy of the mean flow, $B(K_m + \phi_m)$, is positive around the ridge. On the contrary, a ridge flows away to downstream when $B(K_m + \phi_m)$ is negative there. The positive $B(K_m+\phi_m)$ around the blocking is associated with the enhanced negative $B(K_m+\phi_m)$ at the upstream jet due to the intensified mechanical energy flux from the upstream jet. Therefore, it is found that the sign of the flux convergence of mechanical energy around the transient ridge is the threshold for the ridge to become a blocking.

CONTENTS

LIST OF TABLES

LIST OF FIGURES

CHAPTER I
INTRODUCTION

1.1 Previous Studies of Atmospheric Blocking

The speculation that an atmospheric blocking is induced by traveling synoptic disturbances was proposed by meteorologists in the 1950s (e.g., Berggren et al. 1949; Rex 1950). . In the late 1970s, Green (1977) discussed dynamical interpretation of this problem related to the European blocking of July 1976. Shutts (1983) demonstrated, using a barotropic model, that a basic flow with a dipole blocking pattern is maintained by the vorticity advection due to traveling eddies. The concept of the eddy forcing by synoptic disturbances for a blocking, i.e., an eddy straining hypothesis, is a likely candidate for the theory of blocking onset and maintenance, and is supported by many studies in recent years (e.g., Hansen and Sutera 1984; Mullen 1987; Haines and Marshall 1987; Nakamura and Wallace 1990; Tanaka 1991, 1998; Marques and Rao 1999).

It is known that a blocking has an equivalent-barotropic structure. Also, the life-cycle of a baroclinic wave, simulated by Simmons and Hoskins (1978) for the first time, indicates that the structure became barotropic for its decaying period. It may

be possible that the constructive effect of eddies for a blocking is explained within the framework of the barotropic dynamics. Many blocking studies, such as Shutts (1983), Haines and Marshall (1987), and others, employed barotropic models.

On the other hand, many studies suggested that the baroclinic process plays a significant role as well, especially during the period of block formation. Colucci (1985) examined the case of explosive cyclone with a downstream blocking anticyclone. He showed that the blocking was forced by both thermal and vorticity advections. The same result was given by Alberta et al. (1991). Tsou and Smith (**?**) examined height tendencies during the development of a blocking event. They indicated that the temperature advection indirectly influenced the blocking formation through the synoptic and synoptic-planetary interaction, although the direct forcing by the temperature advection was much weaker than that by the vorticity advection. Using a diagnostic method, Lupo (1997), and Lupo and Smith (1998), also found that the temperature advection was important during the formation of some blockings. Using a simple barotropic model with a realistic wavemaker, Tanaka (1998) demonstrated that the onset of blocking is led by a Rossby wave breaking, which is forced by barotropic-baroclinic interactions.

Tanaka and Kung (1988) showed, as a result of the three-dimensional normal mode energetics during the FGGE period, that the conversion from synoptic-scale

baroclinic energy to planetary-scale barotropic energy occurred as a precursor of blocking. This implies the occurrence of barotropic-baroclinic interactions in the blocking formation. Several studies demonstrated that the Pacific and the Atlantic blockings appear independent of each other, so that the blocking is a local phenomenon, from a statistical (Lejenäs and Økland 1983), or a dynamical (Lupo 1997), viewpoint. Therefore, global spectral energetics like Tanaka and Kung (1988) may not represent the characteristics associated with pure blocking activities.

1.2 Previous Works on Energetics Divided in Vertical Mean and Sheared Flows

Kinetic energy conversions between the barotropic and baroclinic flows have been studied since the beginning of 1960s. Wiin-Nielsen (1962) first proposed a set of kinetic energy equations divided in the vertical-mean (barotropic) component and the vertical-shear (baroclinic) component. He evaluated the conversion term between these two components from observed data in January 1959 and found that the conversions have a maximum around zonal wavenumber 7 of synoptic eddies. Wiin-Nielsen and Drake (1965) recomputed for more samples on the basis of finer vertical resolution, and showed that the synoptic eddies were responsible for the major portion of the conversion. In the numerical study, Smagorinsky (1963) used the barotropic-

baroclinic conversion to investigate the energetics of the general circulation.

These primal studies carried out the evaluations from a global point of view, since the results were averaged over the Northern Hemisphere. From a local point of view, some studies have been carried out using a formulation analogous to Wiin-Nielsen's (1962). Alpert (1981) investigated the local energetics for two cyclones over North America. Here, a kinetic energy budget was computed over the domain covering a cyclone. Sheu and Smith (1981) also applied the same energy budget for synoptic waves of various 500-hPa flow regimes over North America. Chen and Yen (1985) showed the horizontal distribution of each term of the kinetic energy equations in the Northern Hemisphere and examined the local maintenance of the barotropic and baroclinic kinetic energies for two models and for observation, averaged from December 1978 to February 1979. They exhibited that the conversion from baroclinic to barotropic kinetic energy was also significant from a local viewpoint. Thus, many of the studies using the barotropic and baroclinic kinetic energy equations have presented a long-term mean, or cases of extratropical cyclones. Yet, there have been few studies of the local energetics dealing with an atmospheric blocking using the barotropic-baroclinic decomposition.

1.3 Objectives

Watarai (2000) examined the characteristics of the Pacific blocking occurred on February 1989 using the framework of barotropic and baroclinic kinetic energy derived from Chen and Yen (1985). It was indicated that there were two maxima of the conversion from barotropic to baroclinic along the western and eastern flanks of the blocking ridge. On the other hand, only the maximum existed along the western flank of the ridge for a non-blocking case occurred on January 1989. In order to verify whether the difference between blocking and non-blocking shown by Watarai (2000) is significant, additional works are required with many blocking and non-blocking cases.

The first purpose of this study is to investigate the general characteristics of the energy conversion from baroclinic to barotropic components associated with the blocking, based on a local energetics. In consequence, the generality of the features found by Watarai (2000) will be confirmed. Secondly, the threshold that a transient ridge becomes a blocking is sought. The result in this study may contribute the progress of blocking forecast. In order to accomplish these tasks, barotropic and baroclinic kinetic energy equations derived by Wiin-Nielsen (1962) and extended by Chen and Yen (1985) are used.

A blocking phenomenon has characteristic spatial and temporal structures. By using such a particularity, a number of studies of the local energetics distinguishes the blocking from other phenomena. For example, Mak (1991) identified the blocking as the intraseasonal component of temporal decomposition. He divided the field variables into three components (seasonal, intraseasonal and high-frequency) and examined the role of interactions among these components in the formation and maintenance of a blocking event. Lupo (1997) considered the horizontal scale of phenomena and partitioned the fields into two components (planetary- and synoptic-scales). On the other hand, the vertical scale decomposition as mentioned above is introduced. Correctly, a blocking pattern has both barotropic and baroclinic components since it is not a perfect barotropic structure, but equivalent-barotropic. The barotropic-baroclinic interactions in the blocking region, therefore, include not only the interaction with eddies of synoptic- and planetary-scales, but the self-interaction of the blocking. However, it is expected that the essence of blocking structure is barotropic and that the barotropic-baroclinic interactions around the blocking ridge are dominated by the interactions with baroclinic synoptic eddies. I'm interested in the behavior of barotropic-baroclinic interactions during the formation of blocking phenomena, and it seems that more study is required.

Chapter II describes the local kinetic energy equations decomposed in vertical

mean and sheared flows. The definitions of blocking event used in this study and the quantification of barotropic-baroclinic interactions are also presented in Chapter II. Chapter III describes the data used in this study. The results of energetics analysis for blocking and non-blocking cases in the North Pacific and in Europe are presented in Chapter IV. Discussion and conclusions are given in Chapter V and VI, respectively.

CHAPTER II
METHODOLOGY

2.1 Local Kinetic Energy Equation

In this study, the local kinetic energy conversions between the barotropic and baroclinic flows, which are called "barotropic-baroclinic interactions", are focused during the formation of the blocking. To examine these interactions, it is necessary to use the kinetic energy equations separated into the two flow components. The pioneering work of this method was performed by Wiin-Nielsen and his colleague (e.g., Wiin-Nielsen 1962, 1967; Wiin-Nielsen and Drake 1965), as mentioned in Section 1.2. In order to examine a blocking with a local viewpoint, the local equations extended by Chen and Yen (1985) are adopted in this study. The brief description of this formulation is displayed below and symbols are listed in Table 2.1.

For each meteorological variable, $\xi = u, v$ or Φ, the barotropic (i.e., the vertical mean) and baroclinic (the vertical sheared) operators are defined by the following:

$$\xi_m = \frac{1}{p_s}\int_0^{p_s} \xi dp, \tag{2.1}$$

$$\xi_s = \xi - \xi_m, \tag{2.2}$$

where p_s is the surface pressure, and subscript m and s represent the barotropic and baroclinic components, respectively.

The kinetic energies of the barotropic and baroclinic components are

$$k_m = \frac{u_m^2 + v_m^2}{2}, \tag{2.3}$$

$$k_s = \frac{u_s^2 + v_s^2}{2}, \tag{2.4}$$

respectively. The total (the sum of barotropic and baroclinic) kinetic energy is then written

$$k = k_m + k_s + \mathbf{V}_m \cdot \mathbf{V}_s. \tag{2.5}$$

The inner-product term, $\mathbf{V}_m \cdot \mathbf{V}_s$, can be eliminated when mass-integrated vertically from the top to bottom of the atmosphere since $((\ )_s)_m = 0$, and then

$$\begin{aligned} K &= \frac{p_s}{g} k_m + \frac{p_s}{g} (k_s)_m, \\ &= K_m + K_s, \end{aligned} \tag{2.6}$$

where the vertically mass-integrated kinetic energy variables are designated by capital K.

The vertically-integrated prognostic equations of the barotropic and baroclinic kinetic energies are given in the pressure coordinate over the sphere by

$$\begin{aligned} \frac{\partial K_m}{\partial t} &= -\frac{p_s}{g}(\nabla \cdot k\mathbf{V}_m)_m - \frac{p_s}{g}\mathbf{V}_m \cdot \nabla\Phi_m - \frac{p_s}{g}\{\mathbf{V}_m \cdot (\mathbf{k} \times \mathbf{V}_s)\zeta_s\}_m \\ &\quad -\frac{p_s}{g}\{(\mathbf{V}_m \cdot \mathbf{V}_s)\nabla \cdot \mathbf{V}_s\}_m + \frac{p_s}{g}\mathbf{V}_m \cdot \mathbf{F}_m, \\ \frac{\partial K_s}{\partial t} &= -\frac{p_s}{g}(\nabla \cdot k\mathbf{V}_s)_m - \frac{p_s}{g}(\mathbf{V}_s \cdot \nabla\Phi_s)_m + \frac{p_s}{g}\{\mathbf{V}_m \cdot (\mathbf{k} \times \mathbf{V}_s)\zeta_s\}_m \end{aligned} \tag{2.7}$$

$$+\frac{p_s}{g}\{(\mathbf{V}_m \cdot \mathbf{V}_s)\nabla \cdot \mathbf{V}_s\}_m + \frac{p_s}{g}(\mathbf{V}_s \cdot \nabla \mathbf{F}_s)_m, \tag{2.8}$$

where $\mathbf{k}$ is a unit vector of vertical direction, $\zeta = \mathbf{k} \cdot (\nabla \times \mathbf{V})$ is the vertical component of relative vorticity, and $\mathbf{F}$ is a frictional forcing vector. Here it is assumed that $\omega = 0$ at the top and bottom of the atmosphere as the boundary condition. Therefore, the barotropic component is nondivergent:

$$\nabla \cdot \mathbf{V}_m = 0. \tag{2.9}$$

On the right-hand side of (2.7), the first term is the convergence of kinetic energy flux by barotropic flow and is represented by $B(K_m)$ hereafter. The second term is the generation of barotropic kinetic energy by barotropic ageostrophic flow $G(K_m)$. The fifth term is the frictional dissipation for barotropic kinetic energy $D(K_m)$. Similarly, on the right-hand side of (2.8), the first, second, and fifth terms are the convergence of kinetic energy flux by baroclinic flow $B(K_s)$, the generation of baroclinic kinetic energy $G(K_s)$, and the dissipation for baroclinic kinetic energy $D(K_s)$, respectively.

Equations (2.7) and (2.8) have an equivalent magnitude but opposite sign for the third and fourth term of the right-hand side, and then they represent the conversion between the barotropic and baroclinic flow, i.e., barotropic-baroclinic interactions, $C(K_s, K_m)$. It is usually positive on the average of a large area. For example, Chen and Yen (1985) estimated the mean value of $C(K_s, K_m)$ over the Northern Hemi-

sphere for a winter (December 1978 to February 1979) using the ECMWF data and obtained a value of 1.33 Wm^{-2}. According to our estimate, using the NCEP/NCAR reanalysis, a similar value of 1.40 Wm^{-2} is obtained for December 1988 to February 1989. Examining the barotropic-baroclinic interaction term in more detail, it is clear that it consists of two parts, nondivergent (C_{ND}) and divergent (C_D); that is,

$$C(K_s, K_m) = C_{ND}(K_s, K_m) + C_D(K_s, K_m), \tag{2.10}$$

where

$$C_{ND}(K_s, K_m) = -\frac{p_s}{g}\{\mathbf{V}_m \cdot (\mathbf{k} \times \mathbf{V}_s)\zeta_s\}_m, \tag{2.11}$$

$$C_D(K_s, K_m) = -\frac{p_s}{g}\{(\mathbf{V}_m \cdot \mathbf{V}_s)\nabla \cdot \mathbf{V}_s\}_m. \tag{2.12}$$

In (2.7), the generation of kinetic energy in the barotropic flow, $G(K_m)$, can be written as

$$\begin{aligned} G(K_m) &= -\frac{p_s}{g}\mathbf{V}_m \cdot \nabla\Phi_m \\ &= -\frac{p_s}{g}\nabla \cdot \Phi_m\mathbf{V}_m \\ &= B(\Phi_m), \end{aligned} \tag{2.13}$$

because of (2.9); that is, $G(K_m)$ is equal to the convergence of geopotential flux in the barotropic flow, $B(\Phi_m)$. Therefore, the sum of the flux convergence of kinetic energy in the barotropic flow, $B(K_m)$, and $G(K_m)$ means the net forcing for K_m across the

lateral boundary. $B(K_m)$ and $G(K_m)$ can be written as

$$\begin{aligned} B(K_m) + G(K_m) &= -\frac{p_s}{g}\{\nabla \cdot (k + \Phi_m)\mathbf{V}_m\}_m \\ &= B(K_m + \Phi_m). \end{aligned} \tag{2.14}$$

The term $(K_m + \Phi_m)$ represents the flux convergence of mechenical energy in the barotropic flow.

On the other hand, the generation of kinetic energy in the baroclinic flow, $G(K_s)$, consists of the convergence of geopotential flux in the baroclinic flow, $B(\Phi_s)$, and the conversion from available potential energy to barockinic kinetic energy, $C(A, K_s)$:

$$\begin{aligned} G(K_s) &= -\frac{p_s}{g}(\mathbf{V}_s \cdot \nabla\Phi_s)_m \\ &= -\frac{p_s}{g}(\nabla \cdot \Phi_s\mathbf{V}_s)_m - \frac{p_s}{g}(\omega_s\alpha_s)_m \\ &= B(\Phi_s) + C(A, K_s), \end{aligned} \tag{2.15}$$

Hence, the sum of the flux convergence of kinetic energy in the baroclinic flow, $B(K_s)$, and $G(K_s)$ is

$$\begin{aligned} B(K_s) + G(K_s) &= -\frac{p_s}{g}\{\nabla \cdot (k + \Phi_s)\mathbf{V}_s\}_m - \frac{p_s}{g}(\omega_s\alpha_s)_m \\ &= B(K_s + \Phi_s) + C(A, K_s). \end{aligned} \tag{2.16}$$

The term $B(K_s + \Phi_s)$ represents the flux convergence of mechanical energy in the baroclinic flow.

Finally, (2.7) and (2.8) can be rewritten as

$$\frac{\partial K_m}{\partial t} = B(K_m) + G(K_m) + C(K_s, K_m) - D(K_m), \quad (2.17)$$

$$\frac{\partial K_s}{\partial t} = B(K_s) + G(K_s) - C(K_s, K_m) - D(K_s), \quad (2.18)$$

and is illustrated with an energy box diagram, as shown in Fig. 2.1.

In this study, the kinetic energy tendency, B, G and C terms in (2.17) and (2.18) is directly calculated using a reanalysis dataset. The dissipation terms, $D(K_m)$ and $D(K_s)$ are evaluated as a residual of (2.17) and (2.18), respectively. $B(K_m + \Phi_m)$ and $B(K_s + \Phi_s) + C(A, K_s)$ are estimated by B and G terms, using (2.14) and (2.16), respectively.

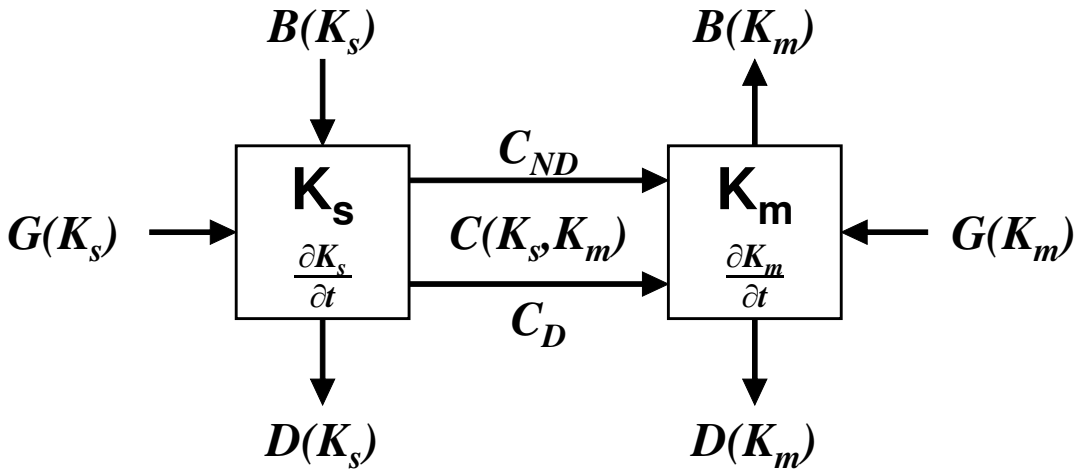

Figure 2.1. The energy box diagram for barotropic and baroclinic kinetic energies. Refer to the text for the definition of variables. Arrows point out the direction of the kinetic energy conversion for a typical baroclinic cyclone (Cyclone II) examined by Alpert (1981).

Table 2.1. List of symbols, variables, constants and definitions.

a	Mean radius of the earth ($= 6.37 \times 10^6$ m)
A	Vertical-integrated available potential energy
$B(\xi)$	Horizontal flux convergence of ξ
c_p	Specific heat of dry air at constant pressure ($= 1004$ J K^{-1} kg^{-1})
$C(\xi, \eta)$	Conversion from ξ to η
$C_D(\xi, \eta)$	Divergent part of conversion from ξ to η
$C_{ND}(\xi, \eta)$	Nondivergent part of conversion from ξ to η
$D(\xi)$	Dissipation of ξ
f	Function
g	Gravity of the earth ($= 9.81$ m s^{-1})
$G(\xi)$	Generation of ξ by ageostrophic flow
h_i	Equivalent depth of vertical mode i
i	Vertical mode number
k	Kinetic energy
$\mathbf{k}$	Unit vector of vertical direction
K	Vertical-integrated kinetic energy
m	Barotropic component (subscript)
p	Pressure
p_s	Surface pressure
R	Gas constant for dry air ($= 287$ J K^{-1} kg^{-1})
s	Baroclinic component (subscript)
t	Time
T	Temperature
u	Zonal wind
v	Meridional wind
$\mathbf{V}$	Horizontal verocity vector; $\mathbf{V} = (u, v)$
z	geopotential height
$\mathcal{Z}_i$	Vertical structure function of vertical mode i
γ	Static stability parameter
ζ	Vertical component of relative vorticity
λ	Longitude
σ	$= p/p_s$
ϕ	Latitude
Φ	Geopotential
ω	Vertical p-velocity
Ω	Earth's angular speed of rotation ($= 7.292 \times 10^{-5}$ rad s^{-1})
$\langle \xi \rangle$	Vertical integration of ξ

2.2 Definition of blocking

In order to pick out a blocking event objectively from a variety of flow patterns in midlatitude, a definition of blocking is required. Rex (1950a; 1950b) defined the blocking event as the followings:

a) the basic westerly current must split into two branches,

b) each branch current must transport an appreciable mass,

c) the double-jet system must extend over at least 45° of longitude,

d) a sharp transition from zonal type flow upstream to meridional type downstream must be observed across the current split, and

e) the pattern must persist with recognizable continuity for at least ten days.

His definition is somewhat lacking in quantification, although it represents the characteristics of the blocking phenomenon with accuracy. Therefore, many researchers modified the Rex's definition as it was convenient for them. For that reason, a variety of definitions were set objectively and quantitatively in many papers (e.g., Dole and Gordon 1983; Lejenäs and Økland 1983; Mullen 1986, 1987; Tibaldi and Molteni 1990).

In this study, two indices of blocking phenomenon are employed. Firstly, the method of Mullen (1986, 1987) is introduced. The Mullen index defines a blocking event as the ridge when the mean 500 hPa geopotential height over the 50 – 60°N belt along a certain longitudinal line is 150 m higher than the average of the nearby 90° longitude sector. Here, the 500 hPa geopotential height is low-pass filtered using the Blackmon et al. (1986) procedure before blocking events are selected. Blackmon filter has the cutoff around frequency (5 days)$^{-1}$. Mullen index with Blackmon filter is evaluated by using only twice daily data at 0000 and 1200 UTC.

Another definition of blocking used in this study was proposed by Lejenäs and Økland (1983). By analogy with zonal index, they defined the 500-hPa height difference between 40°N and 60°N as index:

$$I(\lambda) = Z_{40^\circ\mathrm{N}}(\lambda) - Z_{60^\circ\mathrm{N}}(\lambda), \tag{2.19}$$

where Z is the geopotential height at 500 hPa. The index, $I(\lambda)$, is called as a "B-index" hereafter. When the B-index is negative, as seen for a high-pressure cell staying around 60°N, the situation is considered as a low-index event.

In sections 4.1 and 4.2, a "typical" blocking event is picked up by the superposition of these indices. An example of Hovmöller diagram is shown in Fig. 2.2 on February 1989 when the strong blocking analyzed by Watarai (2000) occurred over

Alaska. In Fig. 2.2, contours represent the Mullen index and shadings are the areas of $I(\lambda) < 0$. Since the area which Mullen index is more than 150 m is almost correspondent to negative B-index around 150°W, it is regarded as the typical blocking. The onset of the typical blocking is defined by the time when Mullen index first exceeds the threshold value of 150 m. The mature time is defined when Mullen index reaches the maximum of the event. In section 4.1, only the typical blockings formed along the 150°W meridian are focused, and the 10 events for 20 winters from 1978/79 to 1997/98 are selected, as shown in Table 2.2. Similarly, the 10 typical blockings along the prime meridian are selected for the same period in section 4.2, as shown in Table 2.3.

In order to identify more blocking events, the only B-index is employed in section 4.3. The onset time of the low-index event is defined in the Hovmöller diagram (not shown) when the B-index first shows a negative value, and a duration is measured by the period for the negative B-index. Here, the index is averaged from $-10°$ to $+10°$ along the longitude to filter small scale noise when the onset and the duration are measured. Added to this, The central longitude is also identified in the Hovmöller diagram where the B-index first shows a negative value, using non-filtered B-index. However, the low-index event is not always regarded as a blocking, because each of the event has a variety of duration. Therefore, a low-index event lasting at least 7

days is defined as a blocking event in this study. Conversely, an event lasting less than 3 days is considered as a non-blocking event. In section 4.3, the low-index events occurred in the North Pacific sector (140°E to 130°W) are picked up. The total of 452 low-index events are extracted during the 51 winters from 1950/51 to 2000/01. Among those, 88 events are identified as blocking and 253 events as non-blocking events.

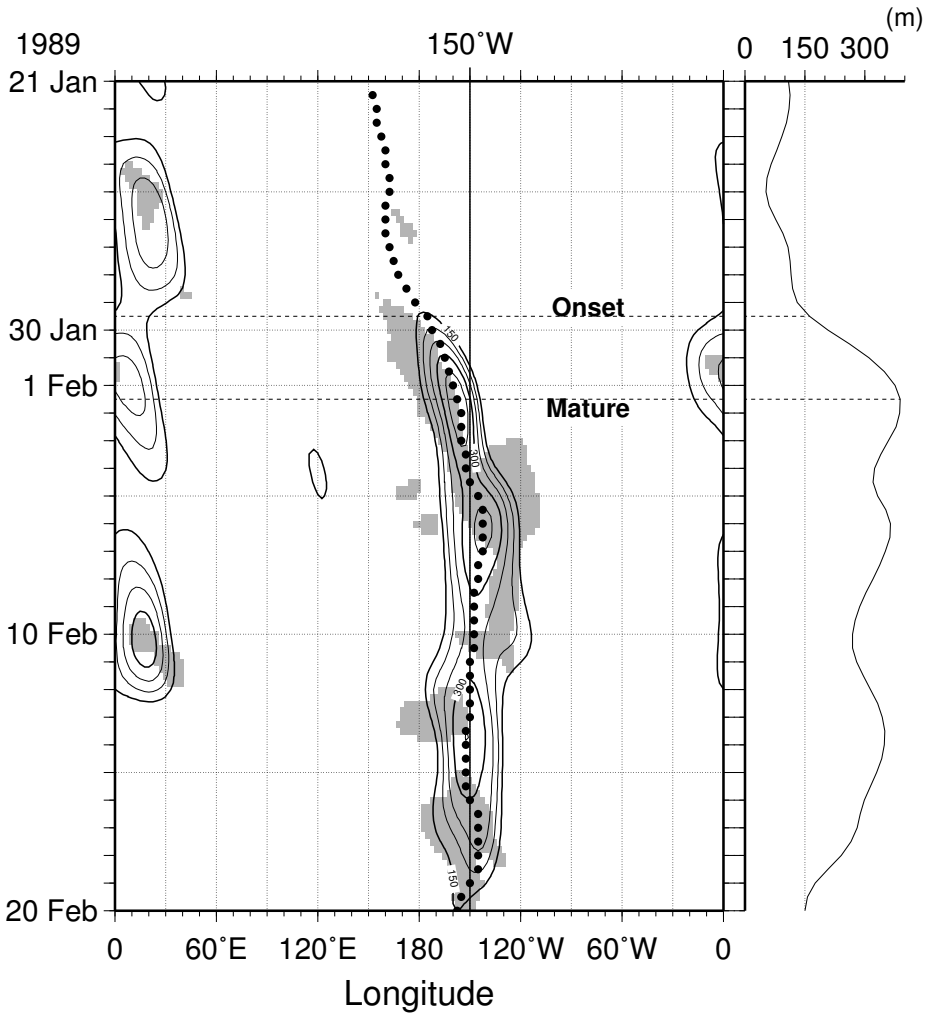

Figure 2.2. An example of a blocking over Alaska taken by two blocking indices (on February 1989, No. 5 in Table 2.2): the solid line whose interval is 50 m shows the magnitude of Mullen's (1987) index, which is illustrated for more than 150 m (i.e. the threshold value), and the shade shows the area where has the negative value of Lejenäs and Øklands' (1983) index. The thick dot line shows the maximum of Mullen index at any instant through the notable blocking. The right panel illustrates the magnitude of Mullen index along the thick dot line.

Table 2.2. A list of the typical blockings over Alaska taken by using both Mullen's (1987) and Lejenäs and Øklands' (1983) indices.

No.	**Onset Time**				**Mature Time**			
1	12Z	2	January	1979	00Z	5	January	1979
2	12Z	31	January	1982	00Z	7	February	1982
3	00Z	15	December	1983	00Z	23	December	1983
4	00Z	28	December	1987	00Z	2	January	1988
5	12Z	29	January	1989	12Z	1	February	1989
6	00Z	19	January	1991	12Z	25	January	1991
7	00Z	23	February	1991	00Z	26	February	1991
8	00Z	13	February	1993	12Z	17	February	1993
9	00Z	28	January	1994	00Z	1	February	1994
10	12Z	24	February	1996	00Z	1	March	1996

Table 2.3. A list of the typical blockings over Europe taken by using both Mullen's (1987) and Lejenäs and Øklands' (1983) indices.

No.	**Onset Time**				**Mature Time**			
1	00Z	17	February	1979	12Z	18	February	1979
2	12Z	18	February	1980	00Z	23	February	1980
3	00Z	3	February	1982	12Z	11	February	1982
4	12Z	30	November	1982	00Z	3	December	1982
5	12Z	28	November	1984	00Z	2	December	1984
6	12Z	7	March	1986	12Z	15	March	1986
7	12Z	13	January	1991	12Z	16	January	1991
8	12Z	24	November	1991	12Z	5	December	1991
9	12Z	23	December	1992	00Z	28	December	1992
10	12Z	3	March	1997	00Z	10	March	1997

2.3 Quantification of Barotropic-Baroclinic Interactions

Watarai (2000) suggested that the barotropic-baroclinic interactions, $C(K_s, K_m)$, played an important role when a blocking occured. In order to represent the intensity of the barotropic-baroclinic interactions around a blocking, a "C-index" is introduced in this study. The value of $C(K_s, K_m)$ is computed by (2.10) at each grid. Since stronger wind makes larger kinetic energy, $C(K_s, K_m)$ tends to have a large magnitude around a blocking compared to that in the blocking. For this reason, the average of $C(K_s, K_m)$ over $-30°$ to $+30°$ in longitude and 50° to 70°N in latitude from the center of the B-index minimum is calculated. The "C-index" is then defined by the time average of that term for 3 days before and after the onset of the low-index event in order to filter the transient noise.

CHAPTER III
DATA

The data used in this study are 6-hourly (0000, 0600, 1200, 1800 UTC) reanalysis provided by the National Center for Environmental Prediction (NCEP)/National Center for Atmospheric Research (NCAR) (see Kalnay et al. 1996). The variables provided by the data set are horizontal wind, $\mathbf{V} = (u, v)$, geopotental height, $z = \Phi/g$, where Φ is geopotential and g is gravitational accerelation, and temperature, T, for 51 winters (November to March) from 1950/51 to 2000/01. The horizontal grid interval of the data is 2.5° lon. × 2.5° lat., and the vertical grids are defined at 17 pressure levels at 1000, 925, 850, 700, 600, 500, 400, 300, 250, 200, 150, 100, 70, 50, 30, 20 and 10 hPa.

The fields separated in barotropic and baroclinic components are mainly focused. In this study, the three-dimensional normal mode expansion technique for discrete data (Kasahara and Puri 1981; Tanaka 1985) is employed to evaluate these components expanded in the vertical normal modes, which manipulates the zonal wind, meridional wind and geopotential height fields. The vertical structure equation, which is obtained by a separation of variables for the linearized primitive equations,

is written as

$$\left(\frac{\partial}{\partial\sigma}\frac{\sigma^2}{R\gamma}\frac{\partial}{\partial\sigma}\right)\mathcal{Z}_i(\sigma)+\frac{1}{gh_i}\mathcal{Z}_i(\sigma)=0, \tag{3.1}$$

where $\sigma = p/p_s$ and h_i is the equivalent depth of i-th vertical mode. $\gamma = (RT_0/c_p) - (dT_0/d\ln\sigma)$ is the static stability parameter, where $T_0 = T_0(p)$ is the global mean temperature, R the gas constant for dry air, and c_p the specific heat at constant pressure. The vertical normal mode functions, $\mathcal{Z}_i(\sigma)$, are the eigenfunctions of (3.1) and satisfy the orthonormal condition; thus it can operate the following transformations:

$$f(\sigma) = \sum_{i=0}^{\infty} f_i\mathcal{Z}_i(\sigma), \tag{3.2}$$

$$f_i = \int_0^1 f(\sigma)\mathcal{Z}_i(\sigma)d\sigma, \tag{3.3}$$

where f is an arbitary function depending on σ. In this study, the vertical modes are truncated from $i = 0$ to 11. The barotropic component is approximated by the barotropic mode (i.e., $i = 0$), and the baroclinic component evaluated by the sum of the baroclinic mode ($i = 1$ to 11).

Geopotential height at 500-hPa level of the NCEP/NCAR reanalysis data is used in order to find blocking events using the indices as mentioned above. To grasp the spatial patterns of compounded fields, geopotential height and potential vorticity (PV) at 250 hPa are mapped. Following the method of Nakamura and Wallace (1993), an approximated form of PV at 250 hPa is calculated by geopotential height field and

temperature fields at 200 and 300 hPa of the reanalysis data.

CHAPTER IV
RESULTS

4.1 Typical Blocking Cases over Alaska

In Watarai (2000), only one strong blocking occurred in Alaska on Februaty 1989 was analyzed, and it was suggested that barotropic-baroclinic interactions related to the blocking formation. In order to verify whether it is a general characteristics, it is important to examine a lot of blockings. In this section, we select the 10 typical blockings over Alaska (around 150°W) using two indices as explained in section 2.2. The compounded 10 blocking events over Alaska are shown in Table 2.2, and includes the event on February 1989.

Figure 4.1 illustrates the composite distributions of (a) K_m and (b) K_s for the 10 typical blockings during the 5-day mean around their mature time. Both K_m and K_s are large at the jet region in Japan. The maximum of K_m is located east of Japan, and its magnitude is about 6.5×10^6 Jm^{-2}. The maximum of K_s is somewhat west and the magnitude is about half of the maximum of K_m. In contrast, the jet around the blocking anticyclone indicates small K_s, suggesting that the flow is mostly barotropic. Both K_m and K_s are obviously small in the center of the blocking, where winds are light.

Figure 4.2 shows the composite distributions of a sequence of 5-day mean $C(K_s, K_m)$ centered at -4, -2, 0, $+2$ and $+4$ days from the mature time, superimposed upon the composite 500 hPa geopotential height fields. Overall, the term $C(K_s, K_m)$ indicates a positive value at almost all the jet regions. A marked maximum is seen over Japan and exceeds more than 20 Wm^{-2}. The position of the maximum lies further west of the maximum of K_s. At the equator side of the maximum, negative area of $C(K_s, K_m)$ is seen, consistent with the result of seasonal mean field by Chen and Yen (1985). When we partition the term $C(K_s, K_m)$ in $C_{ND}(K_s, K_m)$ and $C_D(K_s, K_m)$, as shown in Fig. 4.3, we can find that $C_D(K_s, K_m)$ is comparable to $C_{ND}(K_s, K_m)$ over Japan. The term $C(K_s, K_m)$ shows a dipole structure with positive and negative regions divided by the 30°N line, while $C_D(K_s, K_m)$ indicates positive values over that area. Therefore, these two terms reinforce (offset) each other on the poleward (equatorward) of the jet core.

For the blocking region in Fig. 4.2, there are two maxima of $C(K_s, K_m)$ along the western and eastern flanks of the blocking ridge, which is the same characteristic as the case study by Watarai (2000). The pattern of two maxima is formed prior to the mature time, and slightly intensified as the blocking ridge amplifies (Figs. 4.2a, b). This pattern is most evident when the blockings reach their mature time (Fig. 4.2c). The peak value of the maxima is about 10 Wm^{-2}, which is as small as two-fifths of

that over Japan. After the mature time, the maxima are weakened as the blockings decay (Figs. 4.2d, e). It is important to note that the two maxima in the blocking region mostly can be explained by the nondivergent part of $C(K_s, K_m)$ (Fig. 4.3a). In general, the divergent part of $C(K_s, K_m)$ is nearly zero or even negative in the blocking region (Fig. 4.3b).

Figure 4.4 shows the 5-day mean (-4 to 0 from the mature time) energy box diagram averaged over 165°E–105°W, 60°–80°N, where the local change of K_m appears a marked increase. It corresponds to the developing poleward jet where K_m increases at a rate of 2.26 Wm^{-2} per five days. The maximum contribution for the K_m growth is due to $C(K_s, K_m)$. Although $B(K_m)$ and $G(K_m)$ operate so as to increase K_m, their magnitudes are not more than half of $C(K_s, K_m)$. On the other hand, K_s is principally supplied by $G(K_s)$ and extracted by $C(K_s, K_m)$ and $D(K_s)$. Contribution of $C(K_s, K_m)$ is comparable to that of $D(K_s)$. While $C_D(K_s, K_m)$ contributes the increase of K_s, $C_{ND}(K_s, K_m)$ converts K_s to K_m (not shown). Since the magnitude of $C_{ND}(K_s, K_m)$ is much larger than that of $C_D(K_s, K_m)$, $C(K_s, K_m)$ totally converts K_s to K_m.

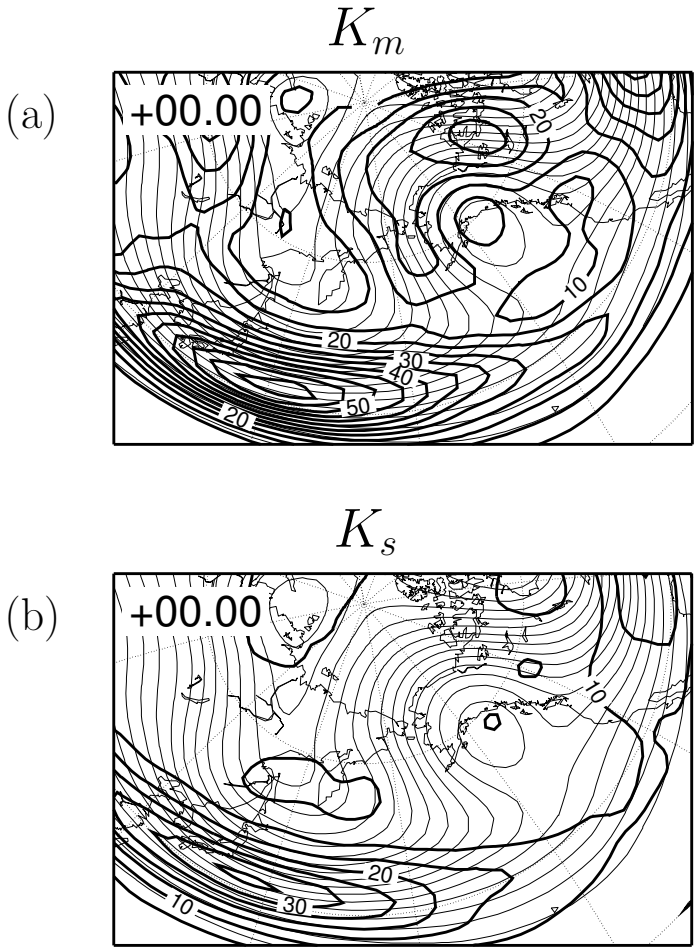

Figure 4.1. Thick solid lines show distributions of 5-day mean (a) barotropic (K_m) and (b) baroclinic (K_s) components of kinetic energy for the mature time. Contour interval is 5×10^5 Jm^{-2}. Thin solid lines show 5-day mean 500 hPa geopotential height with 50 m interval.

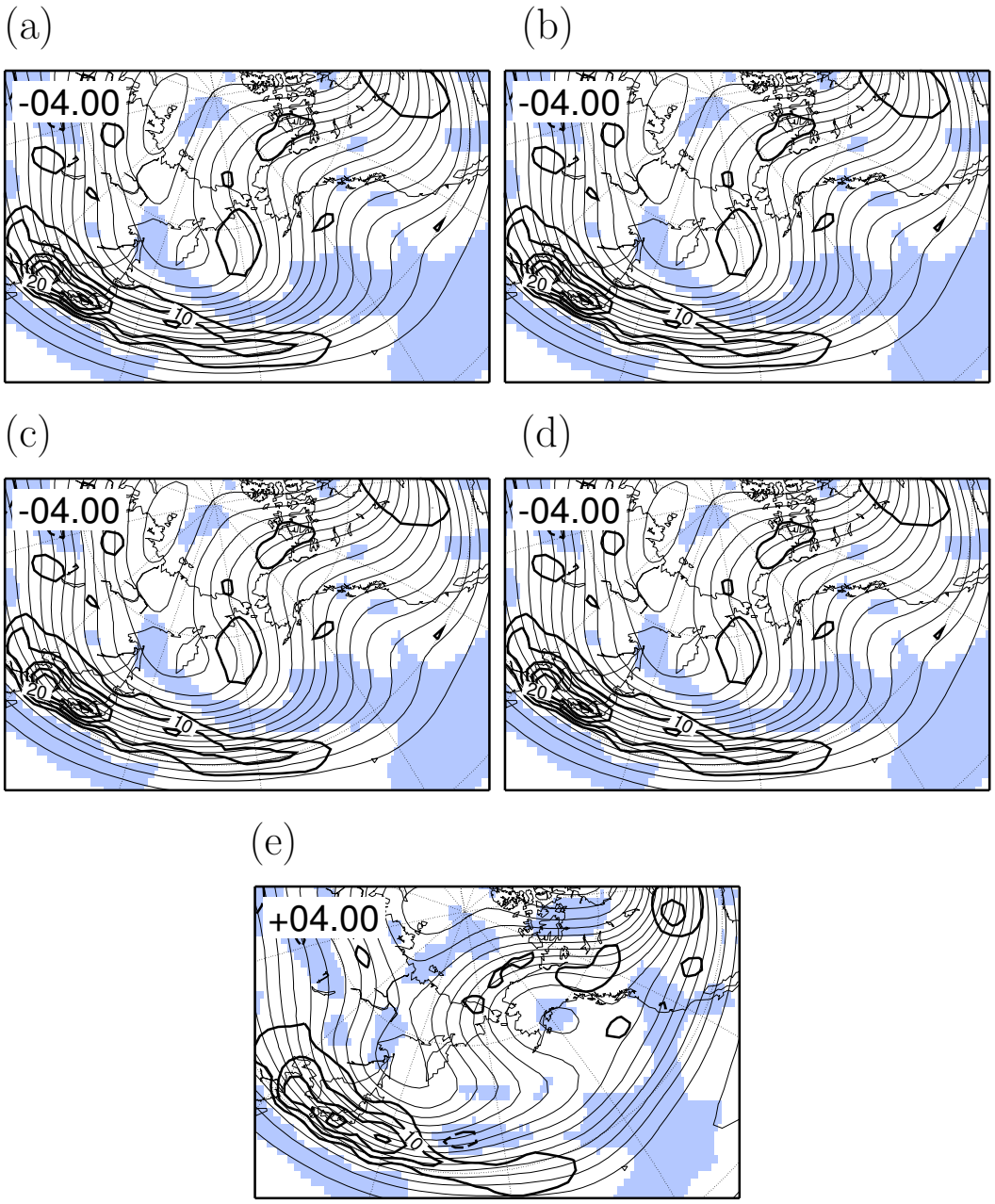

Figure 4.2. Composite distributions of 5-day mean $C(K_s, K_m)$ for the 10 typical blockings over Alaska (about 150°W) at (a) −4, (b) −2, (c) 0, (d) +2 and (e) +4 days relative to the mature time. $C(K_s, K_m)$ is displayed by the thick lines and the shading for negative. Contour interval is 5 Wm^{-2}. Thin solid lines show 5-day mean 500 hPa geopotential height with 50 m interval.

(a) $C_{ND}(K_s, K_m)$

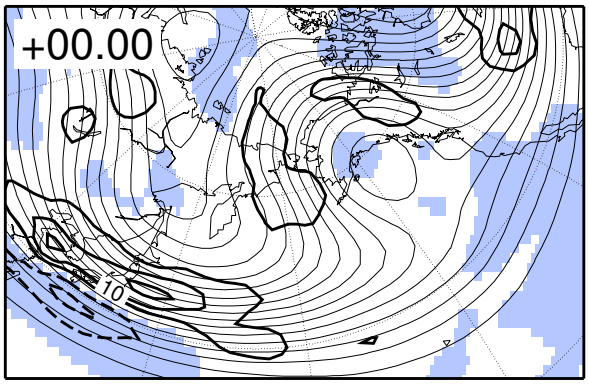

(b) $C_D(K_s, K_m)$

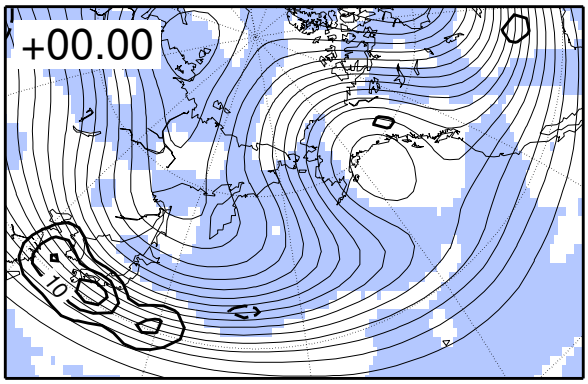

Figure 4.3. Composite distributions of 5-day mean (a) nondivergent (C_{ND}) and (b) divergent (C_D) parts of $C(K_s, K_m)$ for the 10 typical blocking over Alaska (thick lines). Negative values are illustrated by dashed contours and shaded areas. Contour interval is 5 Wm^{-2}. Thin solid lines show 5-day mean 500 hPa geopotential height with 50 m interval.

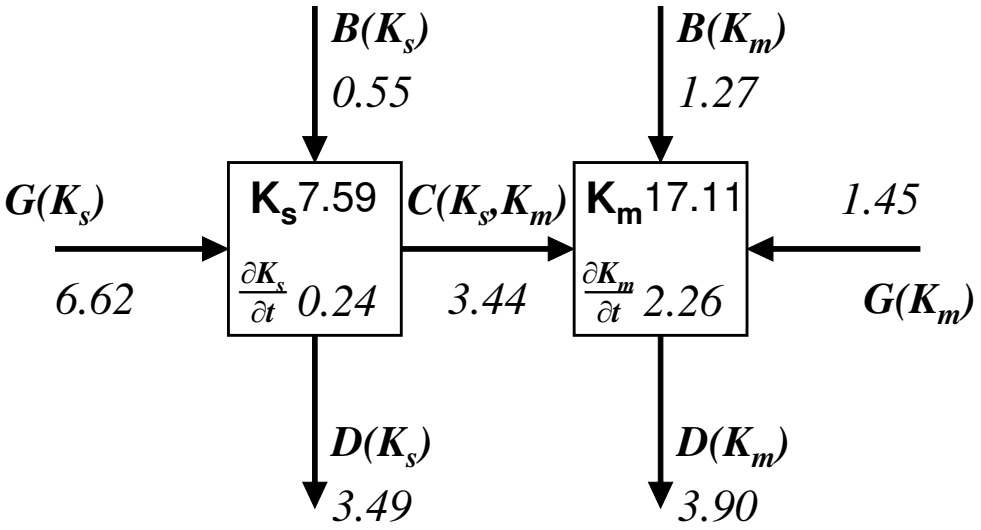

Figure 4.4. 5-day mean (−4 to 0 from the mature time) energy box diagram averaged over 165°E–105°W, 60°–80°N, where the local change of K_m appears a marked increase. Units are 10^5 Jm^{-2} for the kinetic energy variables (K_m and K_s) and Wm^{-2} for the kinetic energy changes.

4.2 Typical Blocking Cases over Europe

As indicated by plenty of climatological studies (e.g., Rex 1950b; Treidl et al. 1981; Lejenäs and Økland 1983; Lupo and Smith 1994), the Euro-Atlantic sector is one of the most preferred blocking regions in the North Hemisphere. In recent years, the difference of blocking formation between the North Pacific and the North Atlantic was suggested in some studies. Nakamura et al. (1997) suggested that the low-frequency quasi-stationary Rossby wave train is primary important in the blocking formation over Europe, whereas the synoptic-wave forcing is necessary for that over the North Pacific. Using local energetics of kinetic energy, it is unknown whether or not the blocking formation is difference between over Alaska and over Europe. In this section, the 10 typical blockings over Europe are thus selected and compared with that over Alaska as shown in the previous section. Selected 10 members over Europe are listed in Table 2.3.

Figure 4.5 illustrates the composite distributions of (a) K_m and (b) K_s for the 10 typical blockings over Europe during the 5-day mean around their mature time. Compounded 500-hPa geopotential height field (thin solid line) shows a blocking anticyclone centered at 5°E. The blocking trough leans in northeast-southwest direction. The jet stream surrounding the blocking is almost barotropic, which is similar to that

over Alaska. In the North Atlantic, the upstream jet is fairly barotropic.

Composite maps of $C(K_s, K_m)$ are illustrated in Fig. 4.6. Although the amplitude of the blocking ridge is somewhat small by contrast with the blocking over Alaska, the pattern of two maxima similar to the Alaskan ridge appears. Unlike to the Alaskan ridge, it seems that the $C(K_s, K_m)$ maximum along the western flank of the ridge corresponds to the effect of the upstream jet. The peak of $C(K_s, K_m)$ around the upstream jet is smaller than that in Japan. Two-maxima pattern around the ridge is maximum at the mature time, as the same over Alaska.

Figure 4.7 shows the 5-day mean (-4 to 0 from the mature time) energy box diagram averaged over 30°W–60°E, 60°–80°N, where the local change of K_m appears a marked increase. Energy flows in the poleward jet over Europe are much similar to that over Alaska (Fig. 4.4). The contribution of $C(K_s, K_m)$ into K_m is significant, which has the value of 3.57 Wm^{-2}. The inflow by $B(K_m)$ is about three times as large as $C(K_s, K_m)$, but most of it balances by $G(K_m)$ outflow. The net boundary effect for K_m (i.e., $B(K_m) + G(K_m)$) is 1.44 Wm^{-2}, which is about 40 % of $C(K_s, K_m)$.

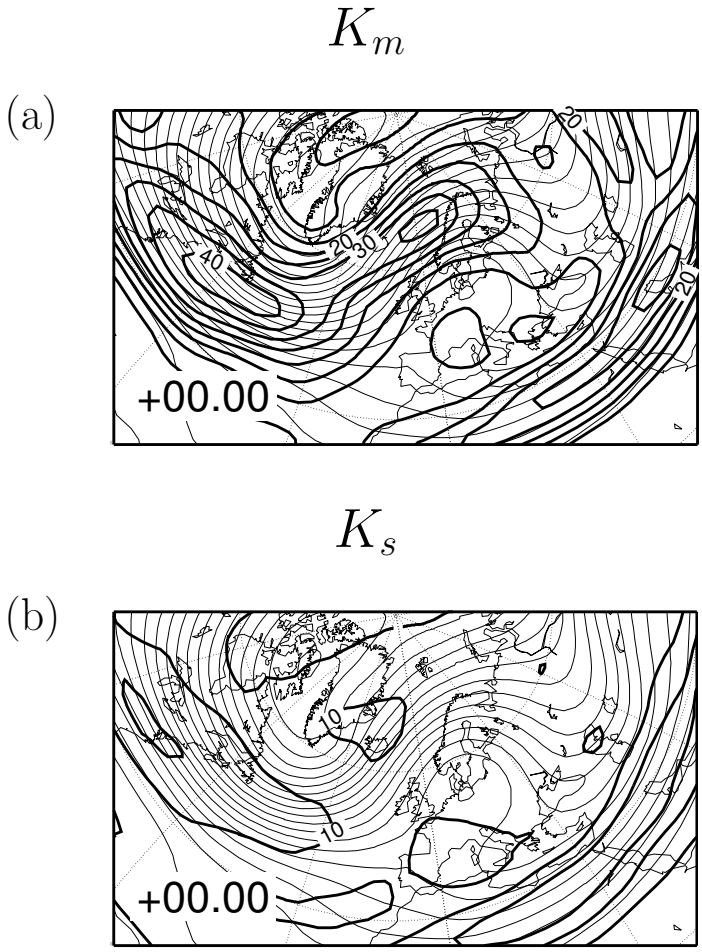

Figure 4.5. Thick solid lines show distributions of 5-day mean (a) barotropic (K_m) and (b) baroclinic (K_s) components of kinetic energy for the mature time. Contour interval is 5×10^5 Jm^{-2}. Thin solid lines show 5-day mean 500 hPa geopotential height with 50 m interval.

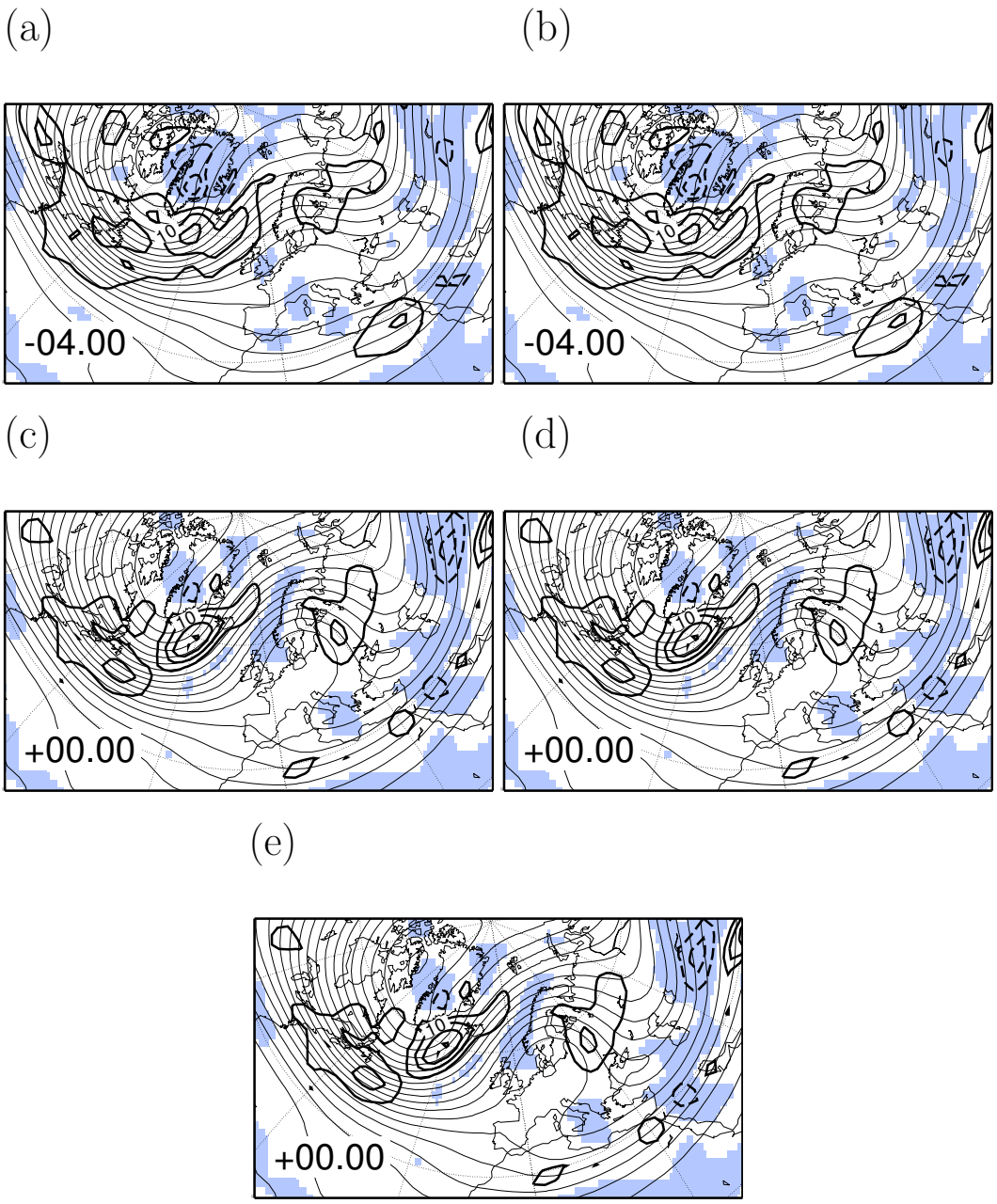

Figure 4.6. As in Figure 4.2 except for the European (about a prime meridian) blocking composite.

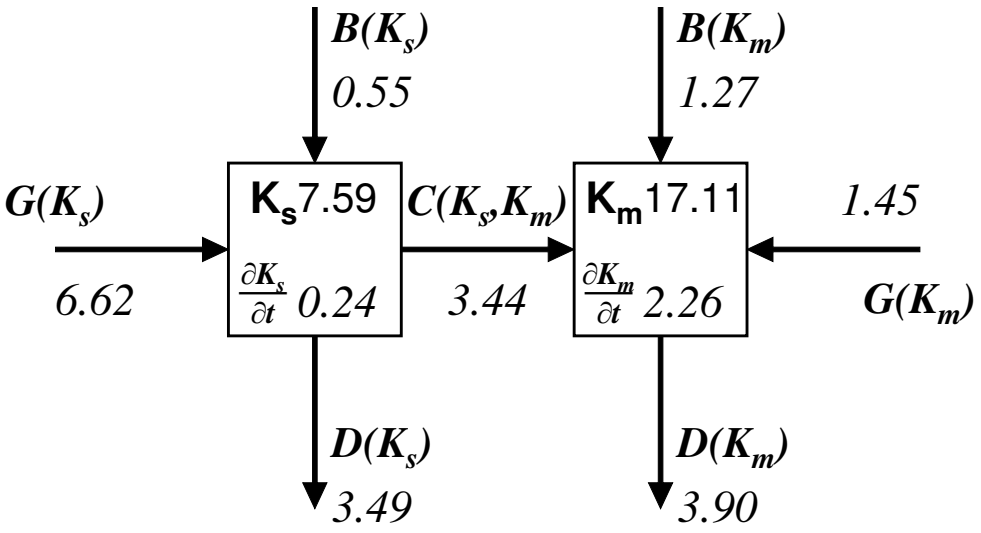

Figure 4.7. As in Fig. 4.4 except for the area averged over 30°W-60°E, 60°-80°N, where the local change of K_m appears a marked increase.

4.3 Comprehensive Energetics of Blockings in North Pacific

In this section, we performed the comprehensive energetics for a large amount of blockings and non-blockings. The only B-index was used in order to pick up these events. The 452 low-index events were identified for 51 winters. Figure 4.8 illustrates the scatterplot between the minimum value of B-index and the duration of the low-index events. It tends that the low-index event lasting longer has lower B-index at the mature time. Correlation coefficient between the duration and the minimum B-index is -0.74 for all the low-index events.

Figure **??** shows the composite maps of 500-hPa geopotential height for the 88 blocking (left) and 253 non-blocking (right) events. They are compounded on the basis of the central longitude, as well as the composite maps hereafter. Before the onset time, the upstream trough around -30° from the central longitude moves eastward and develops equatorward deeply in both the composites. At the onset time, a pair of the trough and the downstream ridge grows up anticyclonically, and the inversion of meridional geopotential-height gradient appears at the central longitude. In the non-blocking composite, the equatorward trough is deeper and the poleward jet is weaker than in the blocking composite. Afterwards, the trough develops further and

a blocking anticyclone is formed at 0° longitude, 60°N in the blocking composite. On the other hand, the trough/ridge pattern decays rapidly and the flow field goes back a zonal regime, as day −4.

Compounded K_m averaged from −2 to +2 from the onset time is illustrated in Fig. 4.10 for (a) the blocking and (b) non-blocking composites. Figures 4.10(a) and (b) are similar each other at first sight. In both composites, K_m has the maximum at the trough region and is quite weak around the ridge. The difference between the blocking and the non-blocking (Fig. 4.10c) shows that the upstream jet around −45° longitude is slightly stronger in the blocking than in the non-blocking. Moreover, the equatorward jet around 0° longitude in the blocking is located in the south of that in the non-blocking. However, the strength of poleward jet around 0° longitude hardly has the difference between the blocking and the non-blocking.

Figure 4.11 shows the composite maps of $C(K_s, K_m)$ averaged from day −2 to +2. In both the blocking (Fig. 4.11a) and the non-blocking (Fig. 4.11b) composites, the maximum of $C(K_s, K_m)$ appears the western flanks of the trough axis (−15° longitude) and the entrance region of upstream jet (−75° longitude), and the latter in the blocking composite is stronger than in the non-blocking. There is a minor peak of $C(K_s, K_m)$ around the ridge in each composites, but the difference (Fig. 4.11c) hardly appears there. The pattern of the difference of $C(K_s, K_m)$ is similar to that

of K_m (Fig. 4.10c) except that $C(K_s, K_m)$ is shifted to the west of K_m.

Thus, it is difficult to find a marked difference between the 88 blocking events and the 253 non-blocking events with regard to the characteristics of $C(K_s, K_m)$ around the ridge. Figure 4.12 illustrates the distribution of the low-index events plotted as functions of the duration of the low-index events and the value of the C-index. Here, the radius of the circle represents the magnitude of the B-index at the mature stage (i.e., the intensity of the event), which is the same as the ordinate in Fig. 4.8, and the C-index quantifies the magnitude of $C(K_s, K_m)$ around the ridge at the onset time, as mentioned in Section 2.3. Regardless of blocking or non-blocking, the low-index events are spread over the C-index from near zero to 8.5 Wm^{-2}. Correlation coefficient between the duration (the intensity) and the C-index is 0.20 (0.27) for all the low-index events. Frequency distributions of C-index for (a) the 88 blocking events, (b) the 452 total low-index events and (c) the 253 non-blocking events are shown in Fig. 4.13. The averages of C-index for the blocking and non-blocking events are 2.75 and 2.07 Wm^{-2}, respectively, and the difference between two groups is less than 1 Wm^{-2}. In both the blocking and the non-blocking, a negative C-index seldom appears. However, small positive values of C-index (0 to 2 Wm^{-2}) are given by a lot of low-index events. Especially, the C-index ranged from 0 to 2 Wm^{-2} account for 52 % (132 events) of the 253 non-blocking cases. The skewness of the non-blocking

events is 0.93, which is twice as large as the blocking cases (0.52), and its distribution is quite unlikely to the normal.

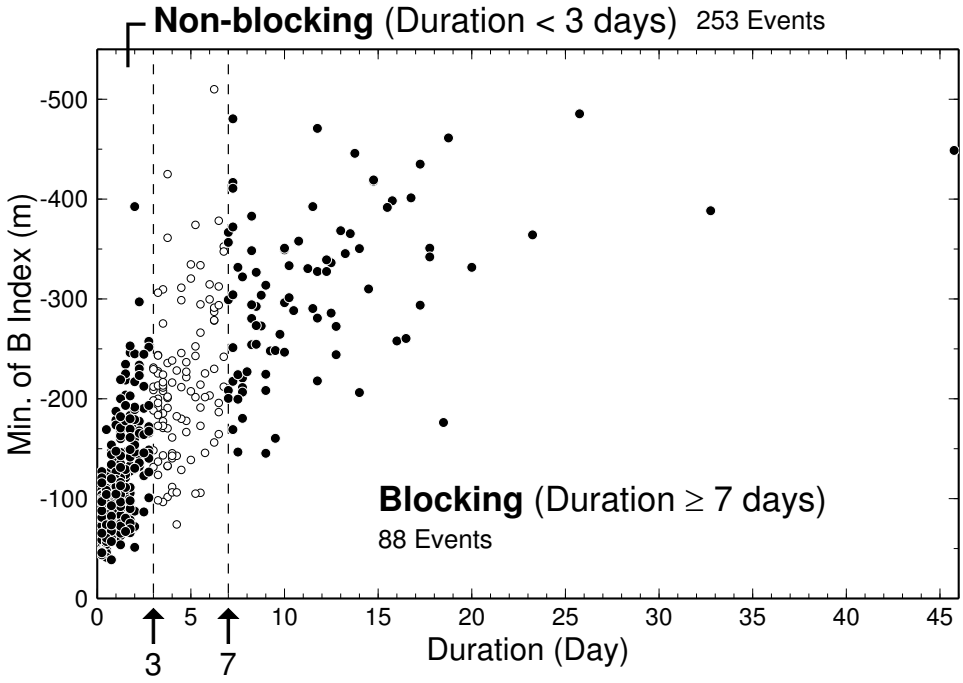

Figure 4.8. Relationship between the duration of negative B-index (abscissa) and the magnitude of B-index at the mature time (ordinate).

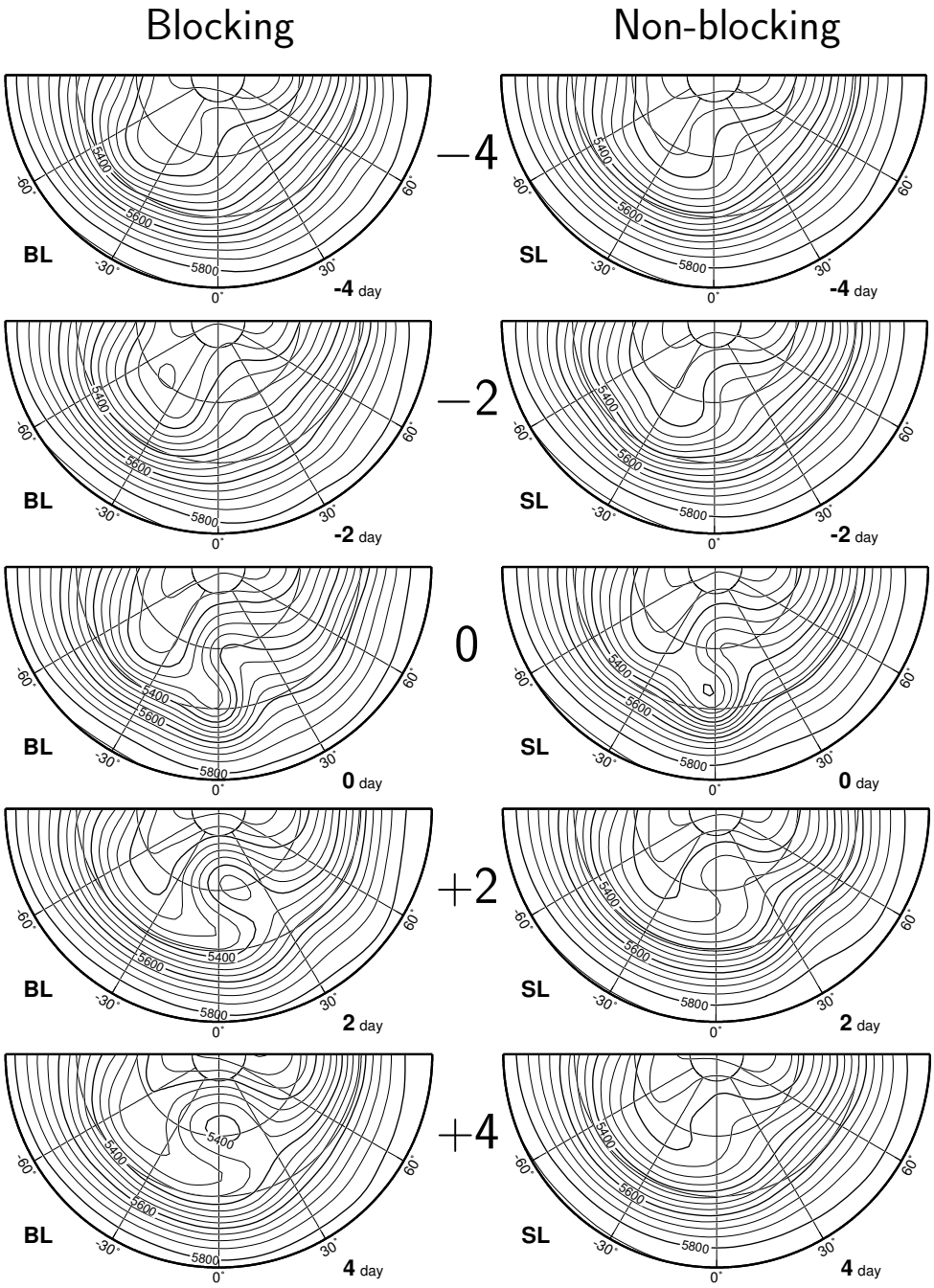

Figure 4.9. Composite maps of geopotential height at 500-hPa level for 88 blocking (left) and 253 non-blocking (right) events, with a range from −90° - 90° of longitude and 20°N - 90°N of latitude. Contour interval is 50 m. Maps at −4 (top), −2, 0, +2 and +4 (bottom) day(s) from the onset time are displayed.

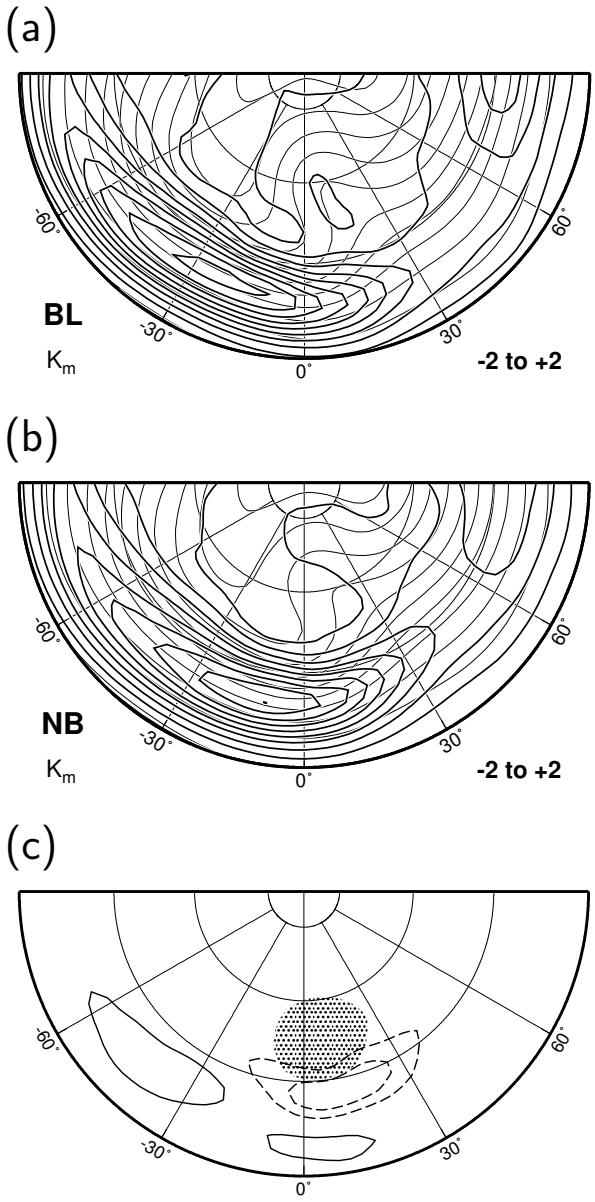

Figure 4.10. Composite maps of the barotropic kinetic energy, K_m, for (a) the 88 blocking events, (b) the 253 non-blocking events and (c) the difference of the blocking and the non-blocking, averaged from -2 to $+2$ days relative to the onset time. Thick solid contours are positive, thick dashed contours are negative, zero contour is omitted, and shaded areas indicate negative values. Contour interval is 5×10^5 Jm^{-2}. Each panel superposes CL composite of 500-hPa geopotential height averaged at the same period (thin solid lines; 75 m interval).

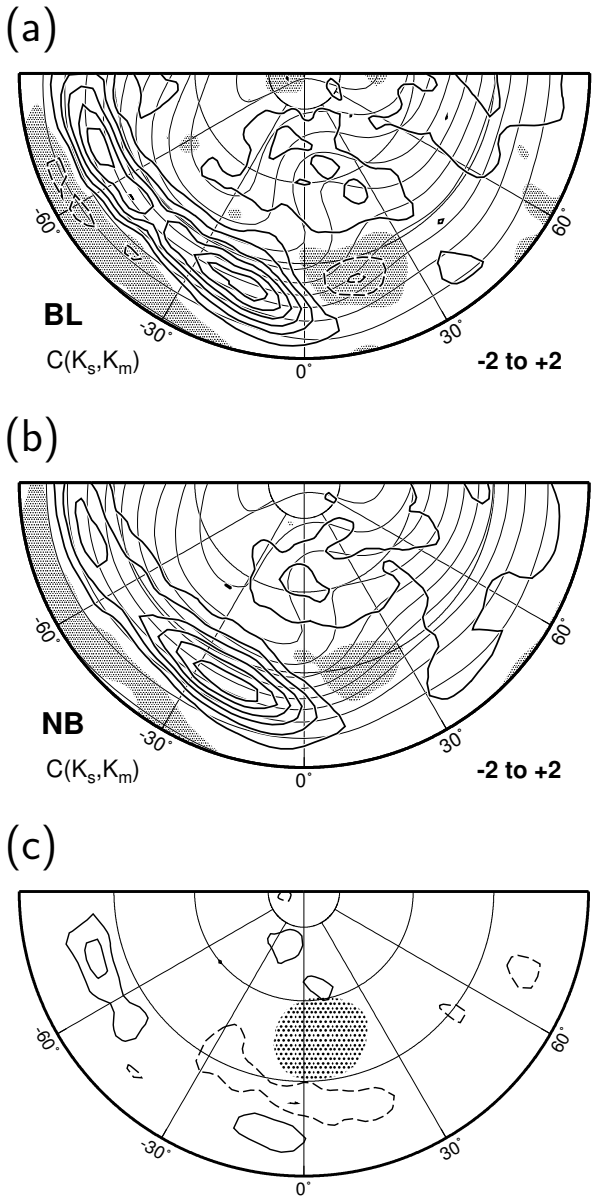

Figure 4.11. Composite maps of the barotropic-baroclinic interactions, $C(K_s, K_m)$, for (a) the 88 blocking events, (b) the 253 non-blocking events and (c) the difference of the blocking and the non-blocking, averaged from -2 to $+2$ days relative to the onset time. Thick solid contours are positive, thick dashed contours are negative, zero contour is omitted, and shaded areas indicate negative values. Contour interval is 2 Wm^{-2}. Each panel superposes CL composite of 500-hPa geopotential height averaged at the same period (thin solid lines; 75 m interval).

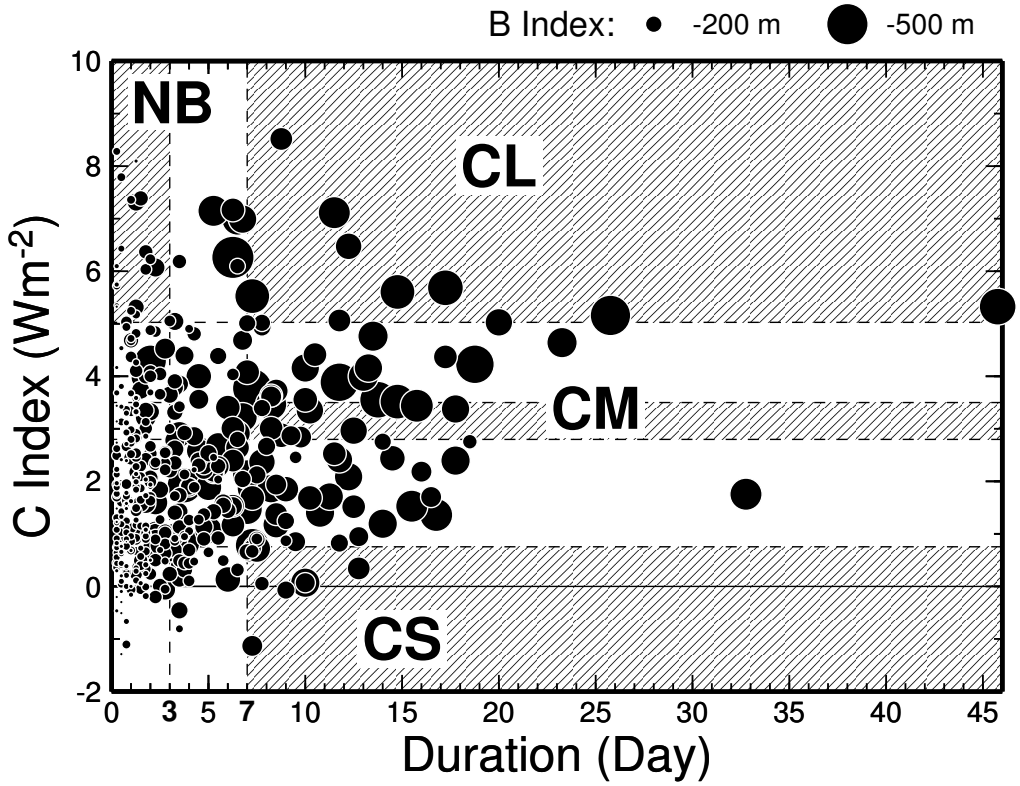

Figure 4.12. Relationship between the duration of negative B-index (abscissa) and the magnitude of C-index (ordinate). A radius of closed circle stands for the magnitude of B-index at the mature time, and its legends are the upper right outside the diagram. The shaded areas labeled CL, CM, CS and NB show the zones of four composites defined in the text.

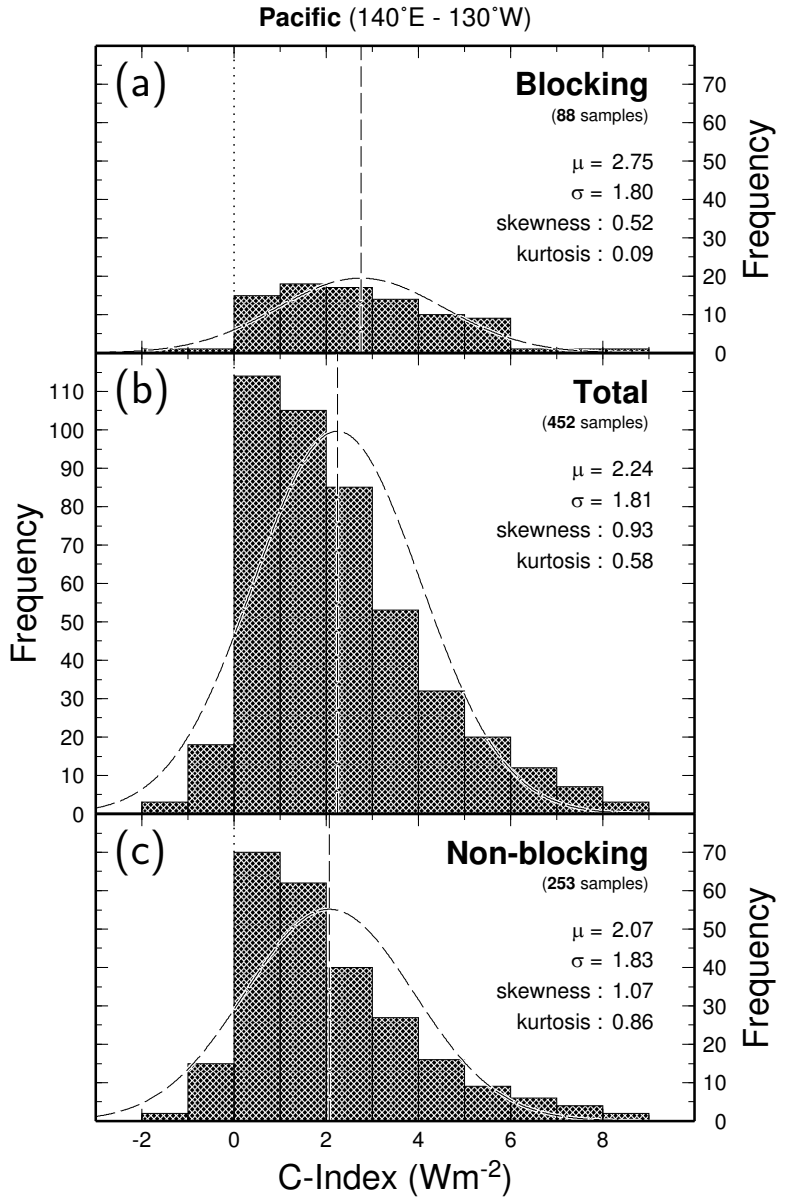

Figure 4.13. Frequency distributions of C-index for (a) blocking, (b) total and (c) non-blocking events. Dashed lines represent the averages of distributions and the corresponding Gaussian distributions.

4.3.1 Sensitivity for barotropic-baroclinic interactions

Clearly in Fig. 4.12, the blocking events with various values of $C(K_s, K_m)$ exist. To examine the features of the blocking patterns with large values of $C(K_s, K_m)$, the blocking cases having the 10 largest C-index are selected and labeled "CL". The value of the C-index is more than 5.02 Wm^{-2} for the CL cases. For comparison, 10 blockings with the smallest C-index are chosen and named "CS", and 10 blockings with the medium C-index as "CM". The mean values of C-index for CM and CS are 3.16 Wm^{-2} and 0.21 Wm^{-2}, respectively. The areas contained in the CL, CM and CS events are shown in Fig. 4.12 CL, CM and CS events are contained in the shaded areas shown in Fig. 4.12 and consists of 10 members listed in Tables 4.1, 4.2 and 4.3, respectively.

Figure 4.14 shows the composite maps of all the CL cases. Left maps show the geopotential height (contour) and the approximated isobaric PV (shade) at 250-hPa level, and right maps show the corresponding barotropic kinetic energy, K_m. All maps are compounded on the basis of the central longitude. There is a small low-PV disturbance about -10° from the central longitude at day -2. The disturbance amplifies rapidly and moves eastward slowly. At day 0 (the onset time), low-PV air thrusts northwestward and the upstream high-PV air southeastward. The inversion

of the north-south PV gradient is formed about 0° longitude. Afterwards, the ridge amplifies more largely, the jet stream splits in north and south, and the Ω-type blocking is formed. The low-PV air corresponding to the blocking is deeply plunged into the poleward air. The blocking formed about 15° longitude is almost stationary. As for K_m, the diffluence of the jet is evident after day 0. In the poleward jet, the maximum value of K_m is about 3.5×10^6 Jm^{-2}, which is comparable with the equatorward jet. K_m around the upstream jet, which is located at −45° longitude, is the most intense at day −2, exceeding 6×10^6 Jm^{-2}, but it reduces to 5×10^6 Jm^{-2} after the onset time.

Figure 4.15 illustrates similar composite maps for CM cases. Likely to CL, a small PV disturbance amplifies rapidly and meridional PV inversion emerges about 0° longitude. Poleward low-PV air is narrower than equatoeward high-PV. After the onset, the ridge becomes still larger and grows more anticyclonically than that in CL. At day +2, the flow pattern like the letter "S" is formed at 0° longitude. This is a typical dipole-blocking pattern. In K_m, the peak at the upstream jet appears at day −2 as in CL, but it is rather weak than that in CL. Although the double-jet structure is formed around 0° longitude after the onset time, the strength of poleward jet is half of that in CL.

The transition of the flow field in CS (Fig. 4.16) greatly differ from CL and CM

in its appearance. The trough at $-30°$ longitude develops rapidly, moves eastward, and arrives at $0°$ longitude about the onset time. The maximum jet is formed at $0°$ longitude rather than at $-45°$ longitude. A weak low-PV thrusts around $+30°$ longitude and is cut off. Isolated low-PV air stays around $0°$ longitude and decays gradually.

Figure 4.17 shows the CL composite maps for the terms in (2.7) and (2.8), averaged from day -2 to $+2$. The tendency of K_m (Fig. 4.17a) is positive around the ridge and negative around the upstream jet. $C(K_s, K_m)$ (Fig. 4.17b) is the largest in the entrance of the upstream jet about $-60°$ longitude. The second maximum of $C(K_s, K_m)$ is seen around the ridge, which is about a half of the upstream jet. Figure 4.17(c) and 4.17(d) show $B(K_m)$ and $G(K_m)$, respectively. The amplitude of $B(K_m)$ and $G(K_m)$ are about 2 to 3 times larger than $C(K_s, K_m)$. There is, however, a strong negative correlation between $B(K_m)$ and $G(K_m)$, as indicated by Chen and Lee (1983) and Chen and Yen (1985). $B(K_m + \Phi_m)$ is shown in Fig. 4.17(e), and the variation of $B(K_m + \Phi_m)$ is comparable with that of $C(K_s, K_m)$. $B(K_m + \Phi_m)$ has a positive contribution along the strong-wind region around the ridge, while it negative on the calm center of the ridge. the upstream jet region corresponds to the strong negative $B(K_m + \Phi_m)$. The distribution of the sum of $B(K_s + \Phi_s)$ and $C(A, K_s)$ (Fig. 4.17f) is similar to $C(K_s, K_m)$. $B(K_s + \Phi_s) + C(A, K_s)$ is almost as large as

$C(K_s, K_m)$ around the upstream jet, but about twice as large as $C(K_s, K_m)$ around the ridge.

Several terms of local energetics for CM composite are shown in Fig. 4.18. The results in CM are equated with that in CL in kind. The local change of K_m (Fig. 4.18a) is large in equatorward jet rather than in poleward jet. The region of positive $C(K_s, K_m)$ forks north and south around $-15°$ longitude (Fig. 4.18b). $B(K_m + \Phi_m)$ is positive around the ridge, but it is smaller in magnitude than that in CL (Fig. 4.18e). As for CS (Fig. 4.19), positive $C(K_s, K_m)$ and $B(K_m + \Phi_m)$ around the ridge are further weak. Conversely, $C(K_s, K_m)$ and $B(K_m + \Phi_m)$ have larger amplitudes over the equatorward jet along 35°N.

Figure 4.20 illustrates the CL composite of the divergent part, $C_D(K_s, K_m)$, and nondivergent part, $C_{ND}(K_s, K_m)$, of the barotropic-baroclinic interactions averaged from day -2 to $+2$. In the entrance region of the upstream jet, $C_D(K_s, K_m)$ is comparable to $C_{ND}(K_s, K_m)$, but that is far smaller than this in all the other regions. $C_{ND}(K_s, K_m)$ is, on the other hand, large around the upstream jet and around the ridge. Along the western flank of the ridge, $C_D(K_s, K_m)$ and $C_{ND}(K_s, K_m)$ have oppposite signs each other, but $C_{ND}(K_s, K_m)$ has the strength enough to ignore $C_D(K_s, K_m)$. On the other hand, both $C_D(K_s, K_m)$ and $C_{ND}(K_s, K_m)$ are positive along the eastern flank of the ridge. This result is consistent with Watarai (2000).

Figures 4.21 and 4.22 show the compounded $C_D(K_s, K_m)$ and $C_{ND}(K_s, K_m)$ for CM and CS, respectively. According to decrease of C-index, wavy $C_D(K_s, K_m)$ becomes active along the 35° longitude jet. Conversely, positive impact due to $C_{ND}(K_s, K_m)$ declines. The decrease of C-index brings the shift of active region from poleward to equatorward.

Figure 4.23 displays the time-latitude cross sections of K_m for three composites, averaged from −30° to 45° longitude. In CL, a double-jet structure is produced after the onset time. a poleward jet around 70°N is comparable with an equatorward jet around 30°N. In contrast, a poleward jet does not appear and a single jet around 30°N is very strong. CM is just intermediate properties between CL and CS. Moreover, the time-latitude cross sections of $C(K_s, K_m)$ and $B(K_m+\Phi_m)$ are shown in Fig. 4.24 and 4.25, respectively. Similarly to K_m, the most active zone of $C(K_s, K_m)$ or $B(K_m+\Phi_m)$ moves from 70°N to 35°N as the C-index decreases. In CL, $C(K_s, K_m)$ is continuously positive at the poleward jet zone (about 65°N) after day −3, and thus accelerates K_m there (Fig. 4.24a). $B(K_m+\Phi_m)$ at the onset time is much intense at 70°N (Fig. 4.25a), and therefore makes a large contribution to the formation of poleward jet. However, the impact on K_m by $B(K_m + \Phi_m)$ in the poleward jet becomes an opposite sense after day +2.5. Similar characteristics appear in CM, although these magnitudes are smaller than that in CL. On the other hand, $C(K_s, K_m)$ is large over the strong

jet at 35°N in CS (Fig. 4.24c). $B(K_m + \Phi_m)$ in the 35° jet is somewhat noisy and strengthens or weakens the equatorward jet periodically.

The relationship between the magnitude of C-index and the pattern of blocking is summarized in Fig. 4.26. When the C-index is large, low-PV thrusts into poleward air deeply and Ω type blocking is formed. When the C-index is medium, meridional scale of the ridge becomes rather small and dipole blocking is constructed. When the C-index is almost zero, cut-off low-PV is very weak, and this pattern is no longer a blocking.

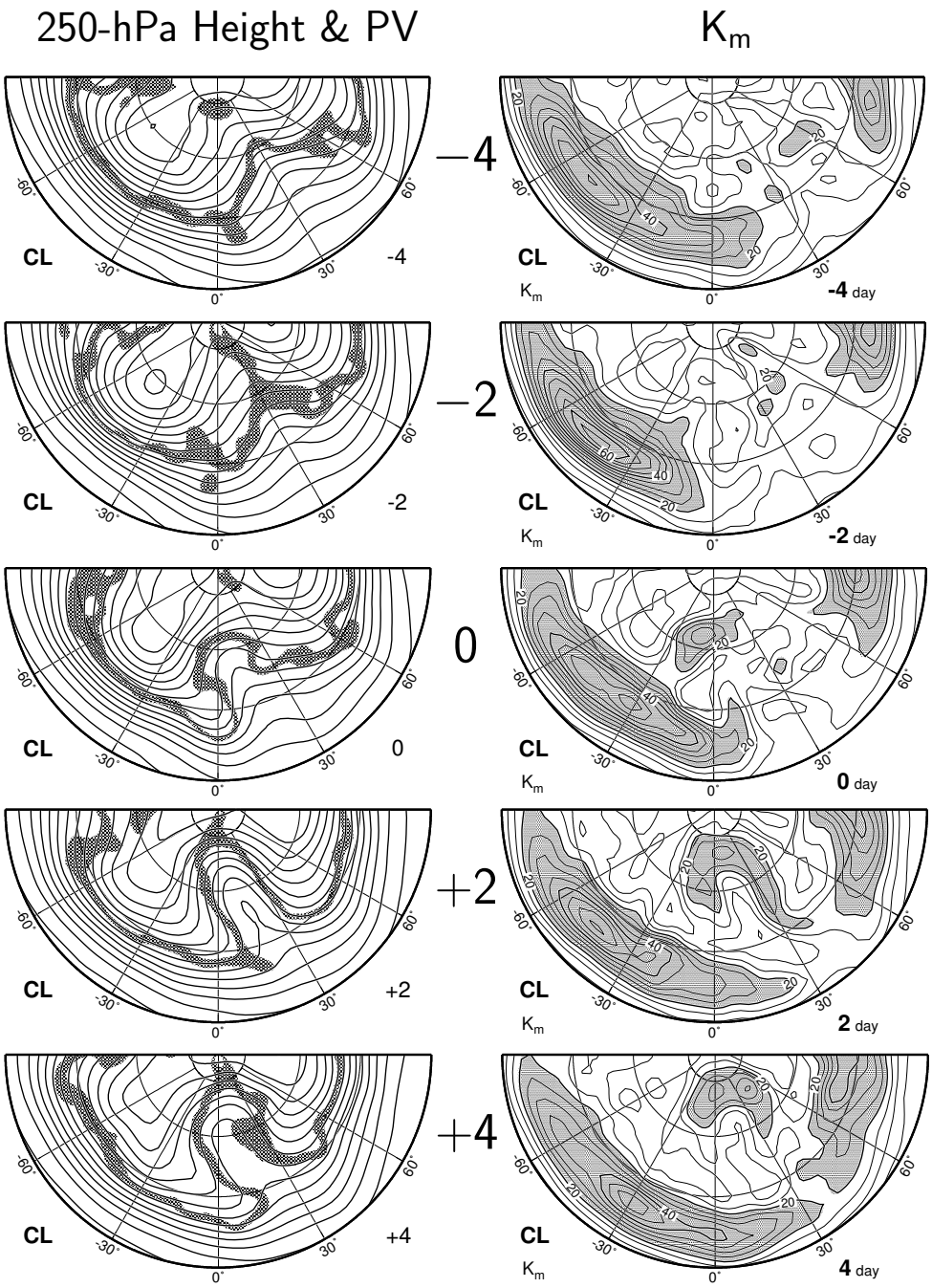

Figure 4.14. CL composite maps of geopotential height at 250-hPa level (left; solid lines) and barotropic kinetic energy, K_m (right; solid lines), with a range from $-90°$ - $90°$ of longitude and 20°N - 90°N of latitude. Shaded areas of left panels show the approximated isobaric PV at 250-hPa level (Nakamura and Wallace 1993), ranged from 3 to 4 PVU ($= 10^{-6}$ m^{2}s^{-1}K kg^{-1}). Shaded areas of right panels denote the values of K_m exceeding 2×10^6 Jm^{-2}. Contour intervals are 100 m in 250-hPa geopotential height and 5×10^5 Jm^{-2} in K_m. Maps at -4 (top), -2, 0, $+2$ and $+4$ (bottom) day(s) from the onset time are displayed.

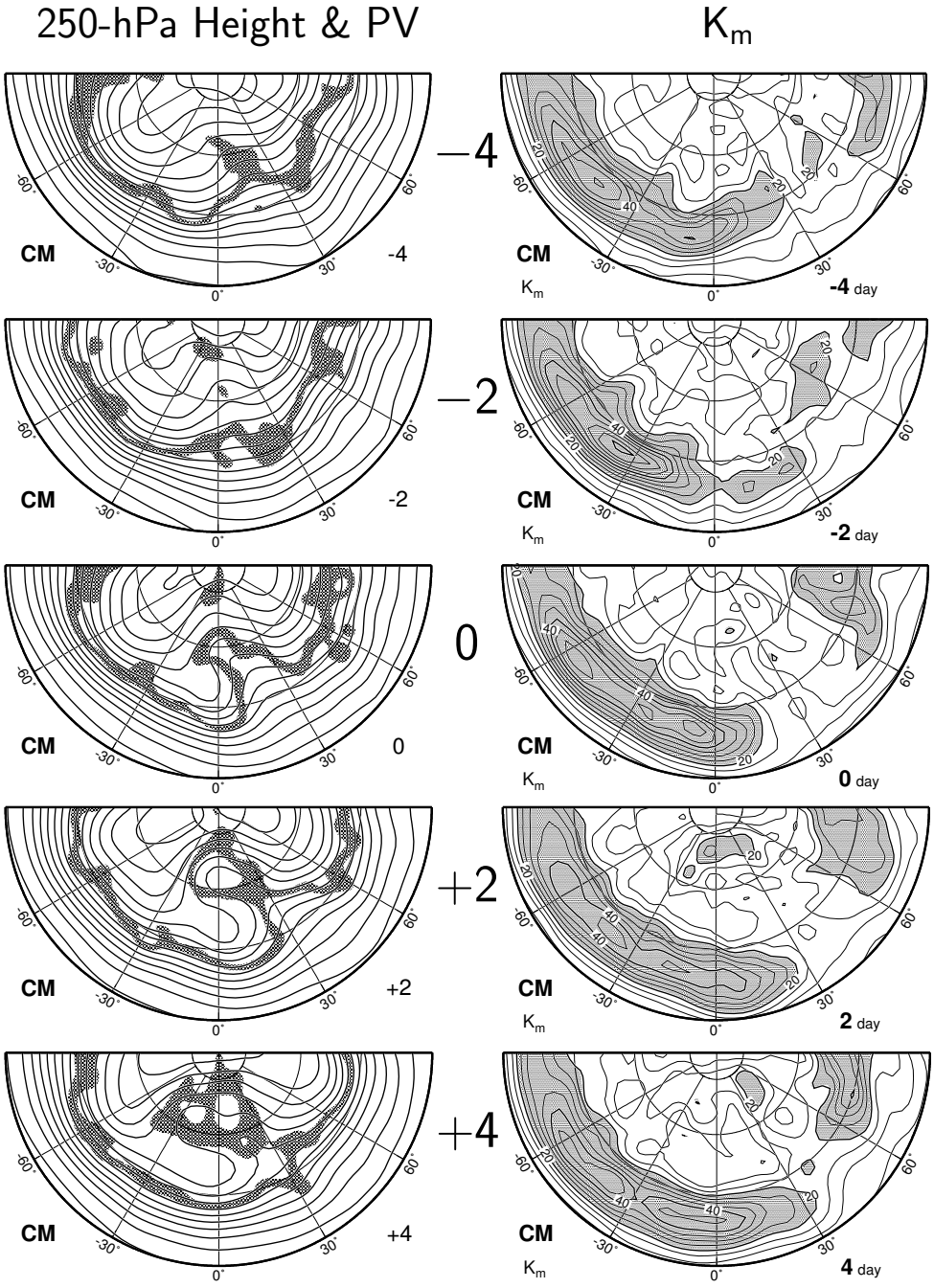

Figure 4.15. As in Fig. 4.14 except for CM composites.

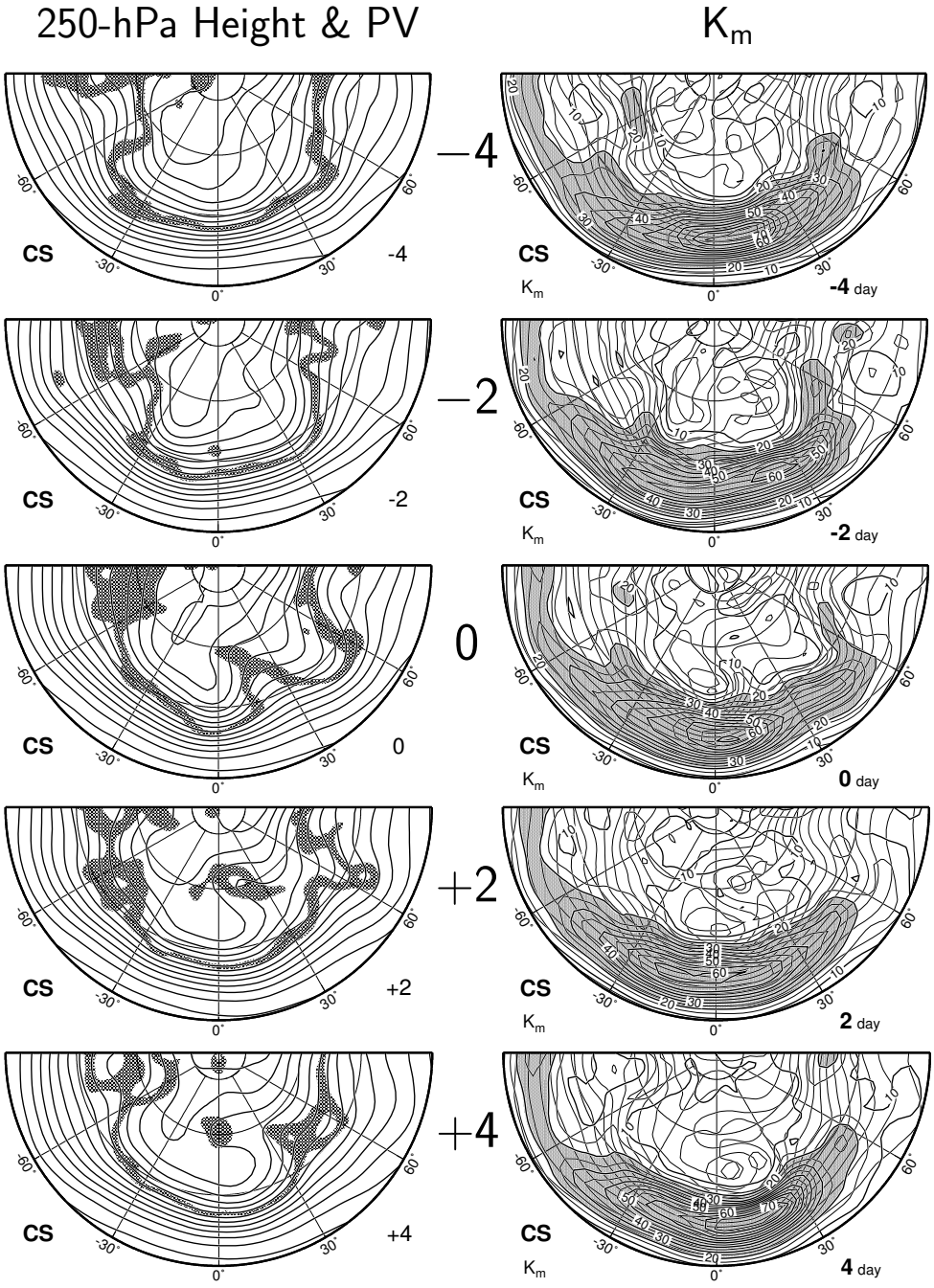

Figure 4.16. As in Fig. 4.14 except for CS composites.

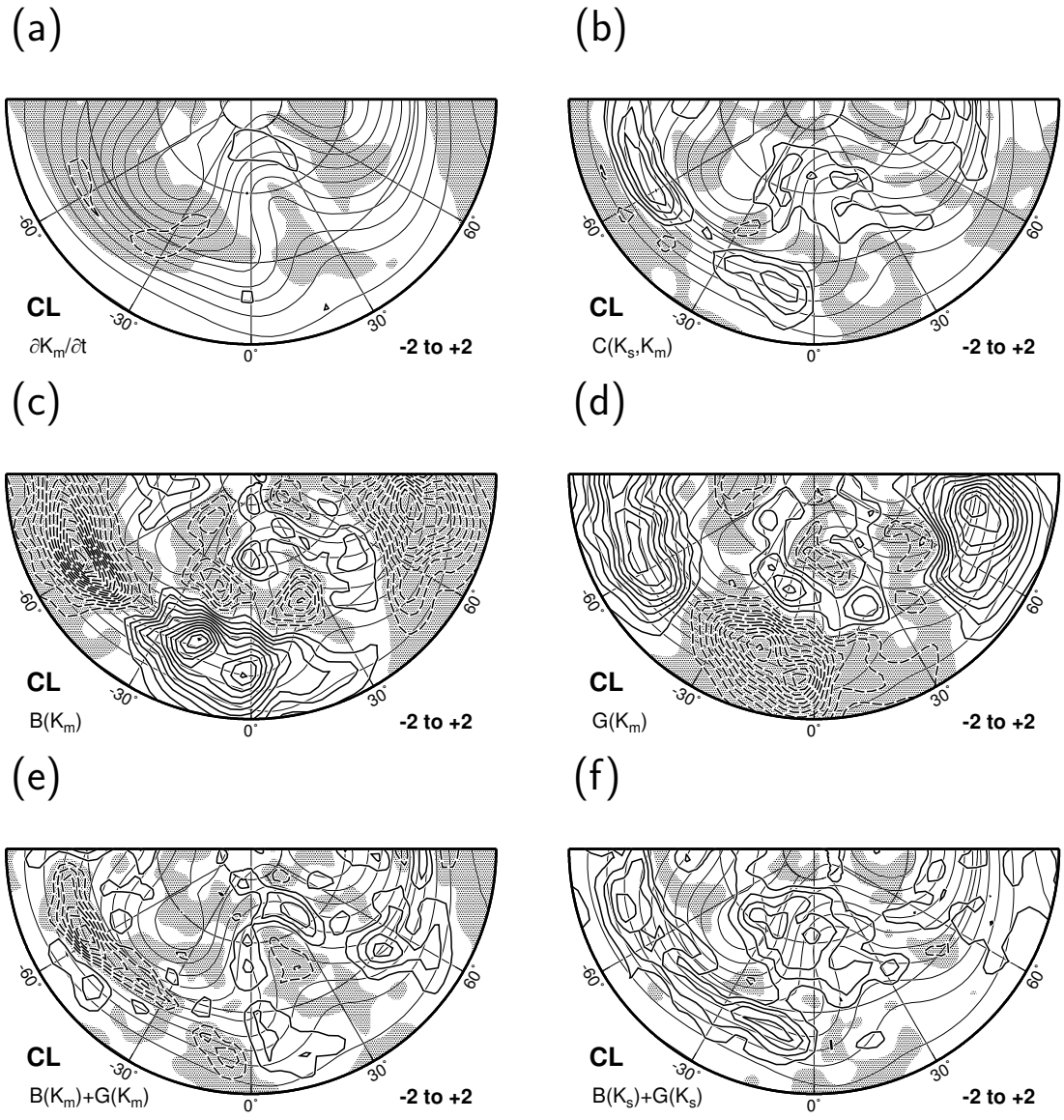

Figure 4.17. CL composite of (a) the tendency of barotropic kinetic energy, $\partial K_m/\partial t$; (b) the barotropic-baroclinic interactions, $C(K_s, K_m)$; (c) the convergence term of kinetic energy flux in the barotropic flow, $B(K_m)$; (d) the generation term of barotropic kinetic energy, $G(K_m)$; (e) the flux convergence of mechanical energy in the barotropic flow, $B(K_m + \phi_m)$; and (f) the sum of the flux convergence of mechanical energy in the baroclinic flow, $B(K_s + \phi_s)$, and the conversion from available potential energy to baroclinic kinetic energy, $C(A, K_s)$, averaged from -2 to $+2$ days relative to the onset time. Thick solid contours are positive, thick dashed contours are negative, zero contour is omitted, and shaded areas indicate negative values. Contour interval is 4 Wm^{-2}. Each panel superposes CL composite of 500-hPa geopotential height averaged at the same period (thin solid lines; 75 m interval).

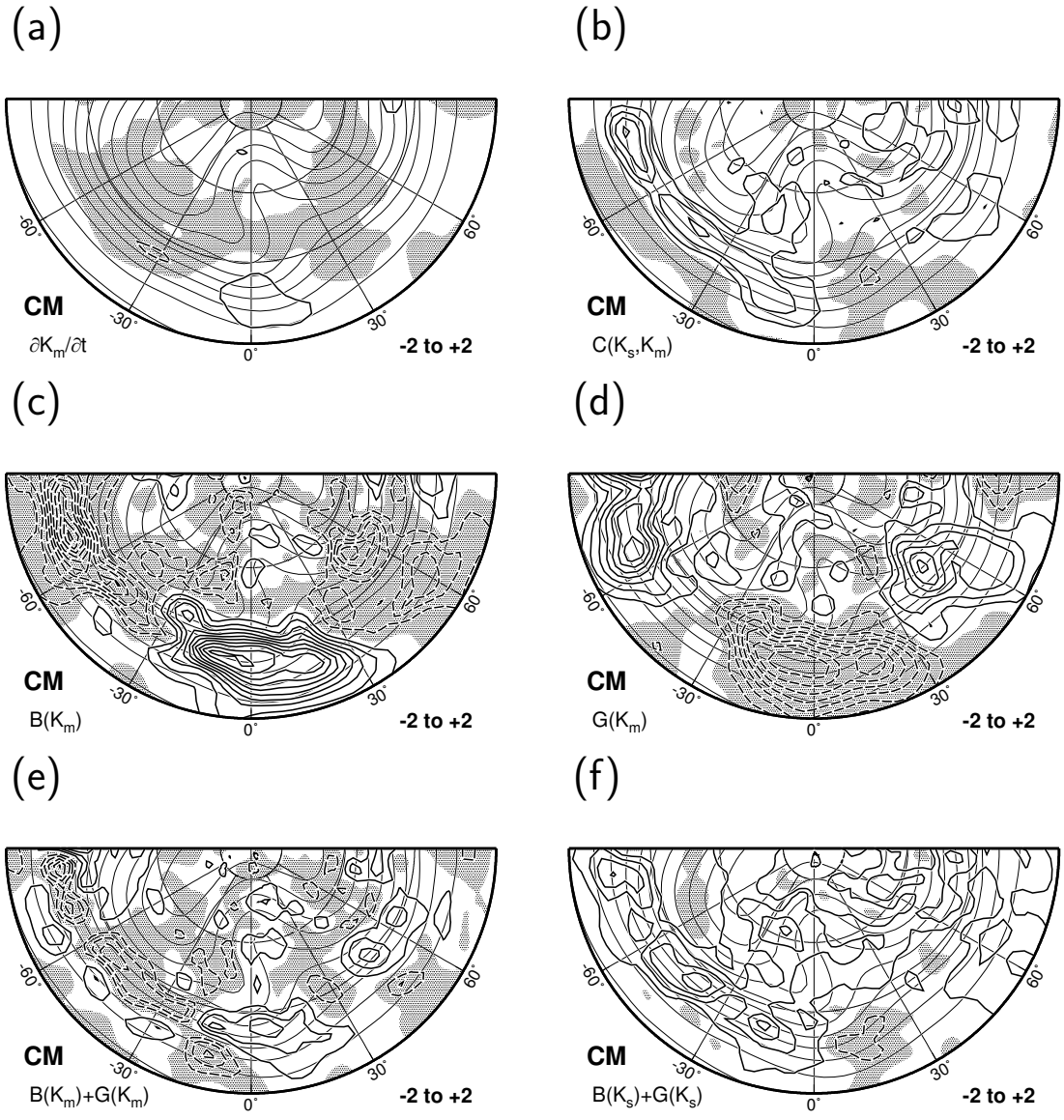

Figure 4.18. As in Fig. 4.17 except for CM composite.

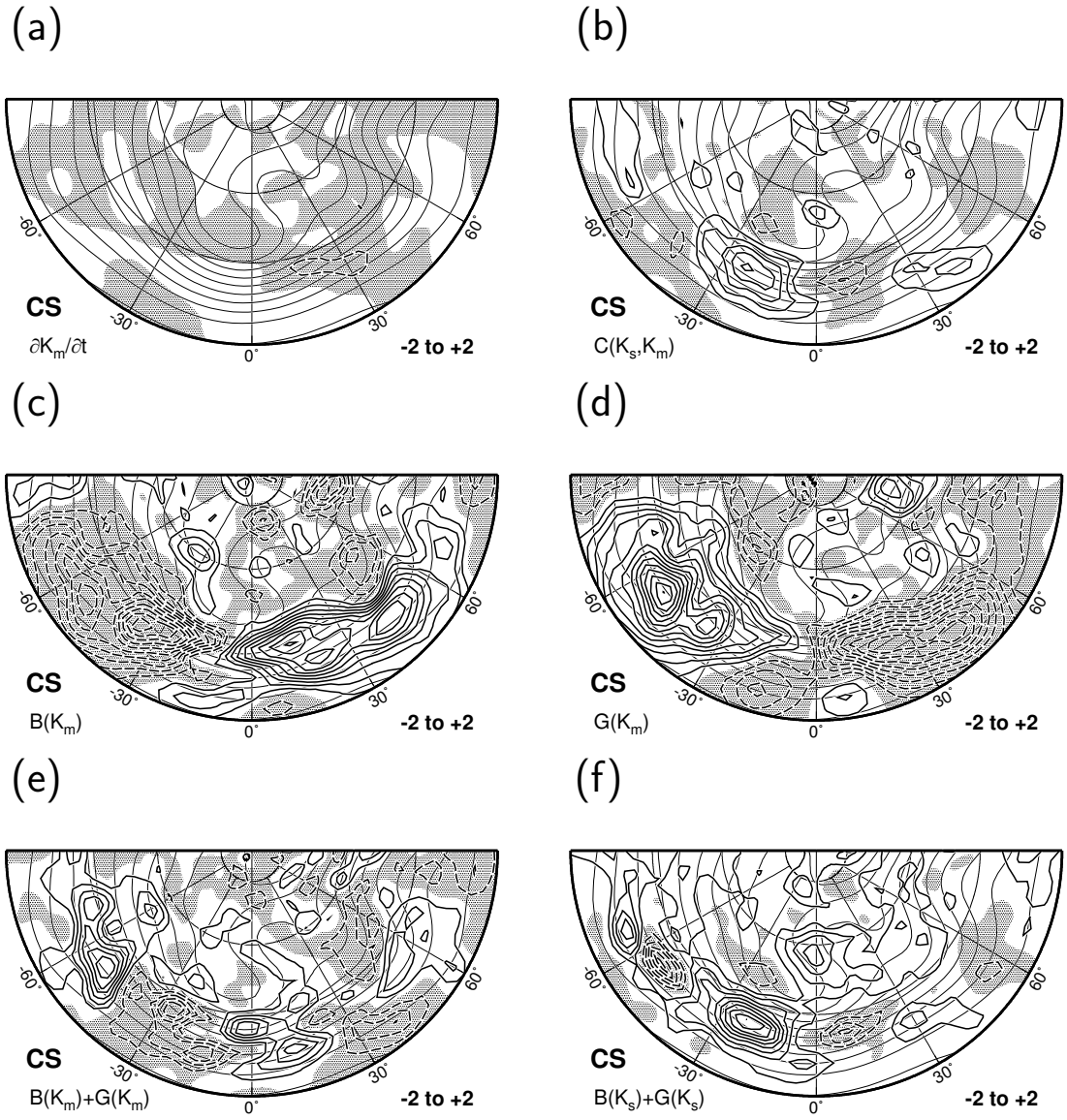

Figure 4.19. As in Fig. 4.17 except for CS composite.

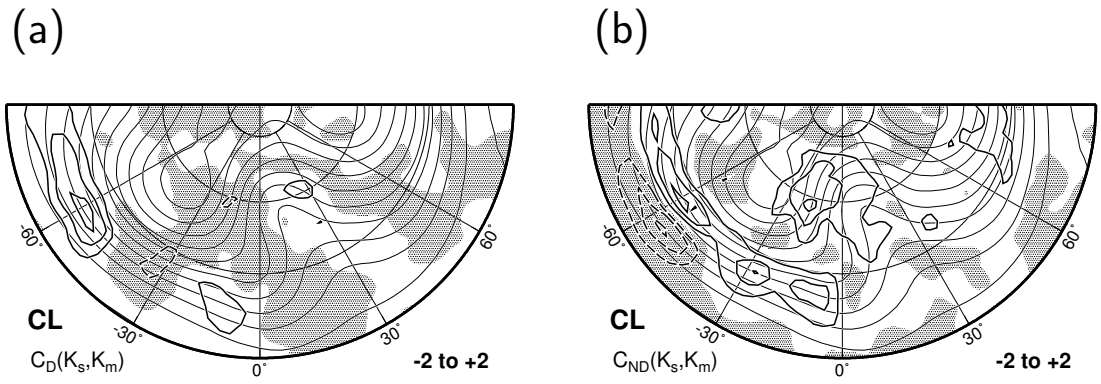

Figure 4.20. CL composite of (a) the divergent part of the barotropic-baroclinic interactions, $C_D(K_s, K_m)$; and (b) the nondivergent part of the barotropic-baroclinic interactions, $C_{ND}(K_s, K_m)$ averaged from -2 to $+2$ days relative to the onset time. Thick solid contours are positive, thick dashed contours are negative, zero contour is omitted, and shaded areas indicate negative values. Contour interval is 4 Wm^{-2}. Each panel superposes CL composite of 500-hPa geopotential height averaged at the same period (thin solid lines; 75 m interval).

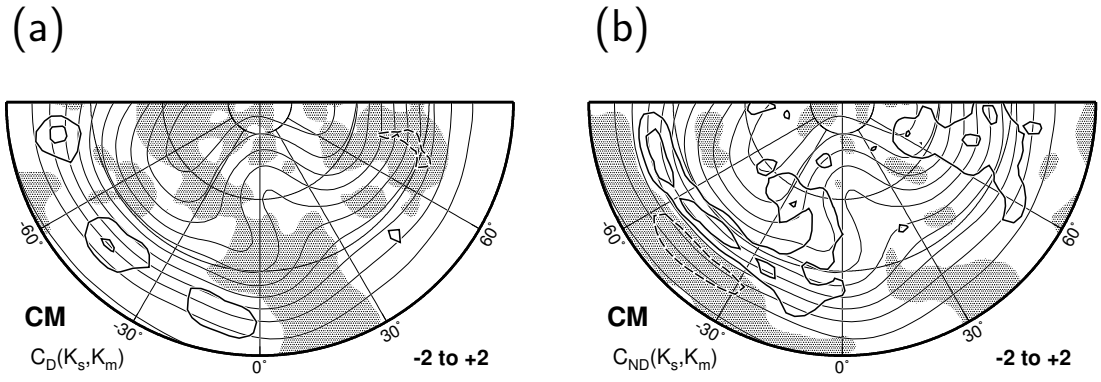

Figure 4.21. As in Fig. 4.20 except for CM composite.

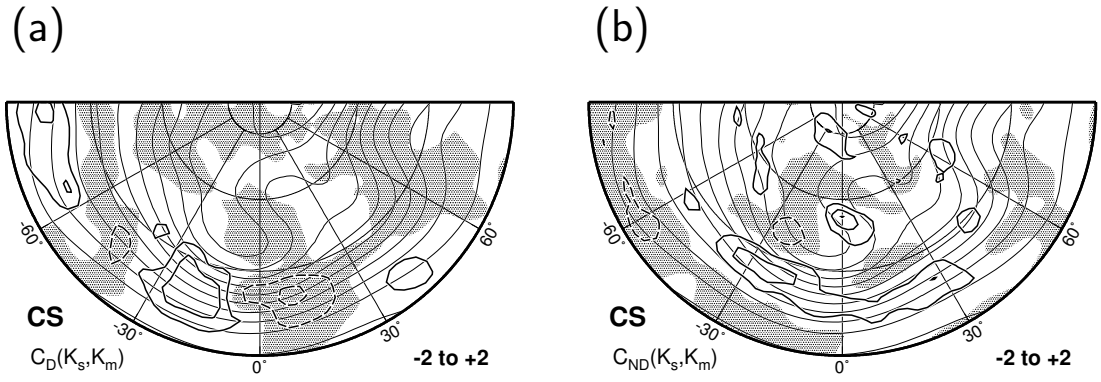

Figure 4.22. As in Fig. 4.20 except for CS composite.

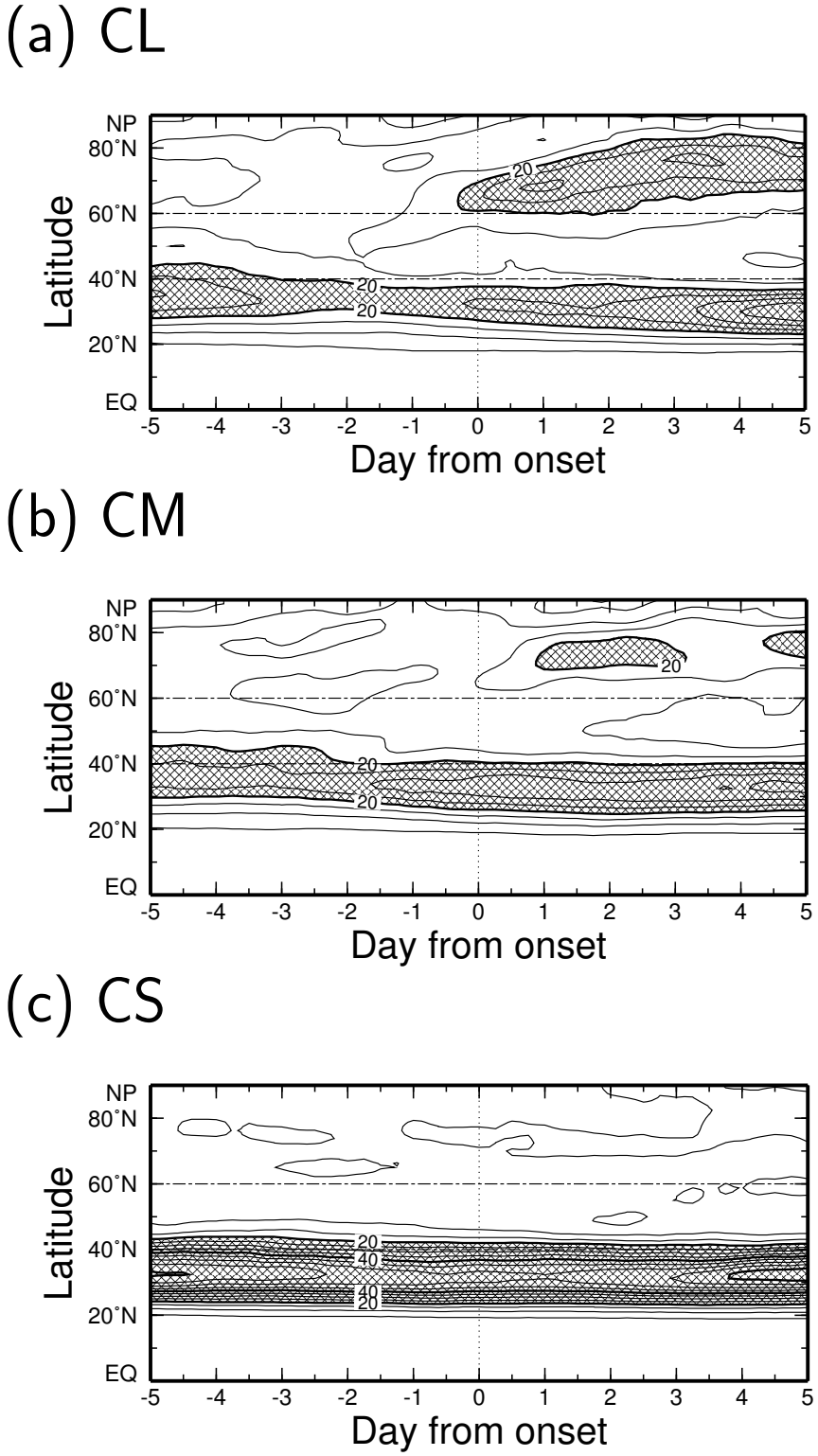

Figure 4.23. Time-latitude cross sections of barotropic kinetic energy, K_m, for (a) CL, (b) CM and (c) CS composites averaged from $-30°$ to $45°$ of latitude. Contour interval is 5×10^5 Jm^{-2} and shading represents the area of $K_m \geq 2 \times 10^6$ Jm^{-2}.

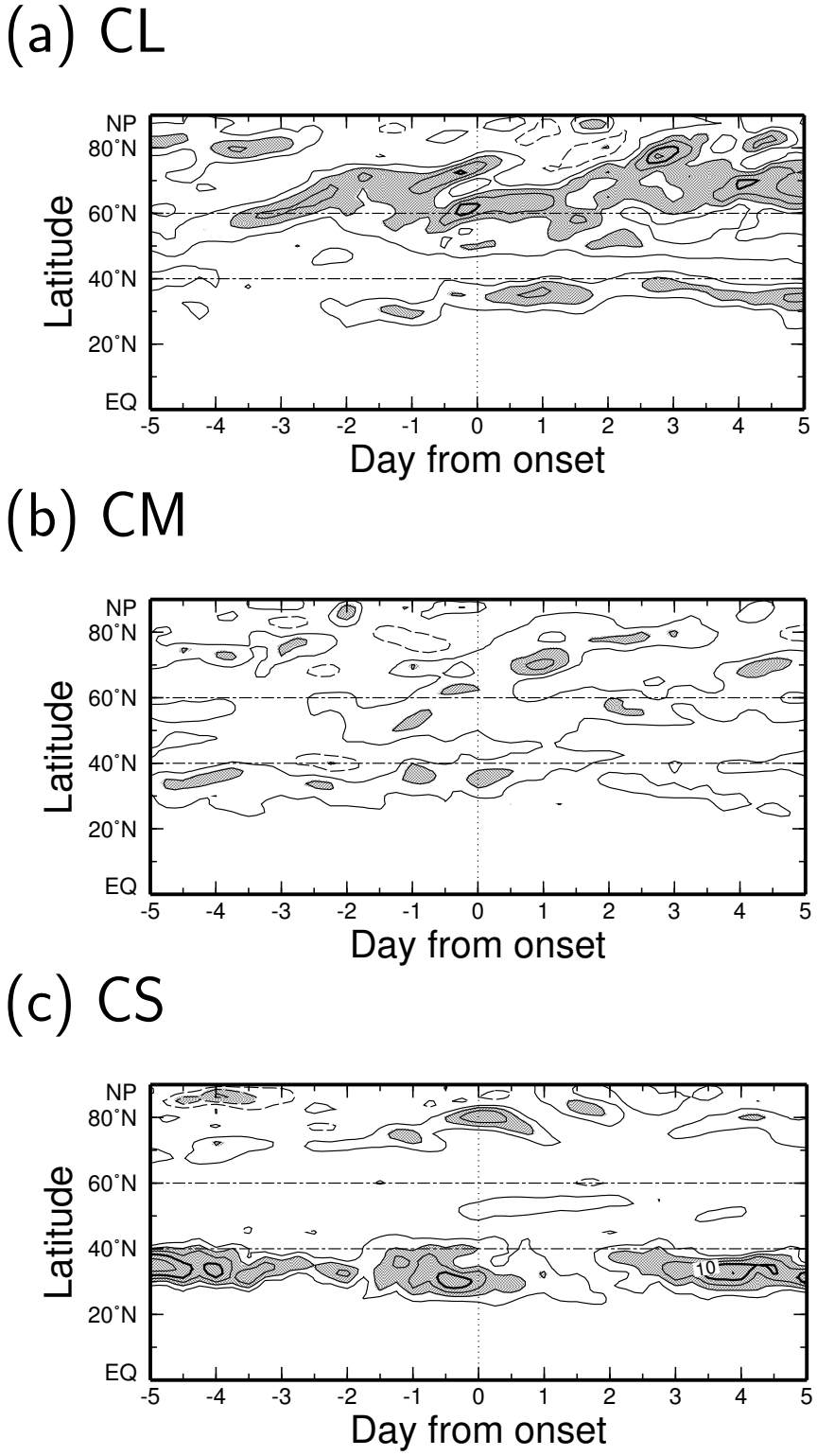

Figure 4.24. Time-latitude cross sections of the barotropic-baroclinic interactions, $C(K_s, K_m)$, for (a) CL, (b) CM and (c) CS composites averaged from $-30°$ to $45°$ of latitude. Contour interval is 2.5×10^5 Jm^{-2} and shading represents the area of $K_m \geq 5 \times 10^5$ Jm^{-2}.

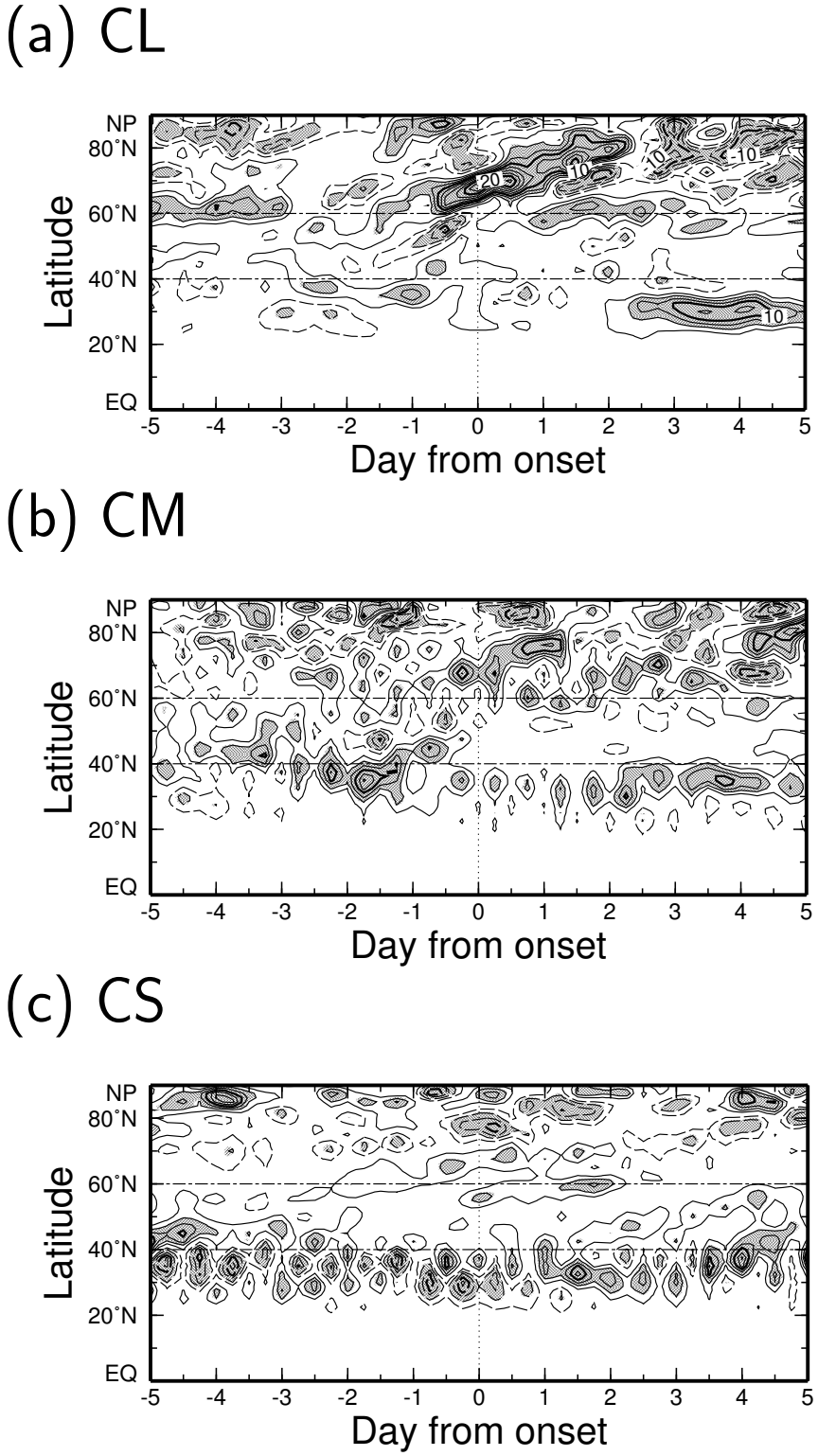

Figure 4.25. Time-latitude cross sections of the flux convergence of mechanical energy in the barotropic flow, $B(K_m+\phi_m)$, for (a) CL, (b) CM and (c) CS composites averaged from $-30°$ to $45°$ of latitude. Contour interval is 2.5×10^5 Jm^{-2} and shading represents the area of $K_m \geq 5\times10^5$ Jm^{-2}.

Table 4.1. A list of CL events.

No.	**Onset Time**				**Central Longitude** (deg)	**Duration** (day)	**Mature B-index** (m)	**C-index** (Wm^{-2})
1	12Z	12	March	1967	185.0	8.75	-273.12	8.52
2	00Z	20	December	1996	185.0	11.50	-392.34	7.12
3	06Z	25	January	1991	202.5	12.25	-327.30	6.48
4	00Z	18	December	1983	200.0	17.25	-435.03	5.68
5	12Z	3	December	1956	195.0	14.75	-418.03	5.61
6	06Z	17	December	1964	175.0	7.25	-416.73	5.53
7	12Z	25	December	1962	190.0	45.75	-448.70	5.33
8	18Z	16	January	1984	150.0	25.75	-485.59	5.16
9	18Z	10	February	1980	207.5	11.75	-280.74	5.06
10	18Z	31	December	1973	197.5	20.00	-331.86	5.02

Table 4.2. A list of CM events.

No.	**Onset Time**				**Central Longitude** (deg)	**Duration** (day)	**Mature B-index** (m)	**C-index** (Wm^{-2})
1	06Z	28	November	1966	207.5	8.25	-382.77	3.47
2	18Z	19	January	1954	197.5	15.75	-398.50	3.44
3	00Z	27	January	1986	192.5	7.75	-206.62	3.39
4	06Z	31	January	1988	202.5	17.75	-342.04	3.38
5	00Z	18	November	1977	192.5	10.25	-333.31	3.35
6	00Z	17	November	1985	192.5	8.25	-294.12	3.01
7	06Z	29	January	1989	162.5	12.50	-336.17	2.96
8	06Z	2	January	1979	207.5	8.75	-303.73	2.87
9	00Z	2	February	1958	220.0	9.25	-247.74	2.87
10	06Z	27	January	1951	172.5	9.75	-264.68	2.84

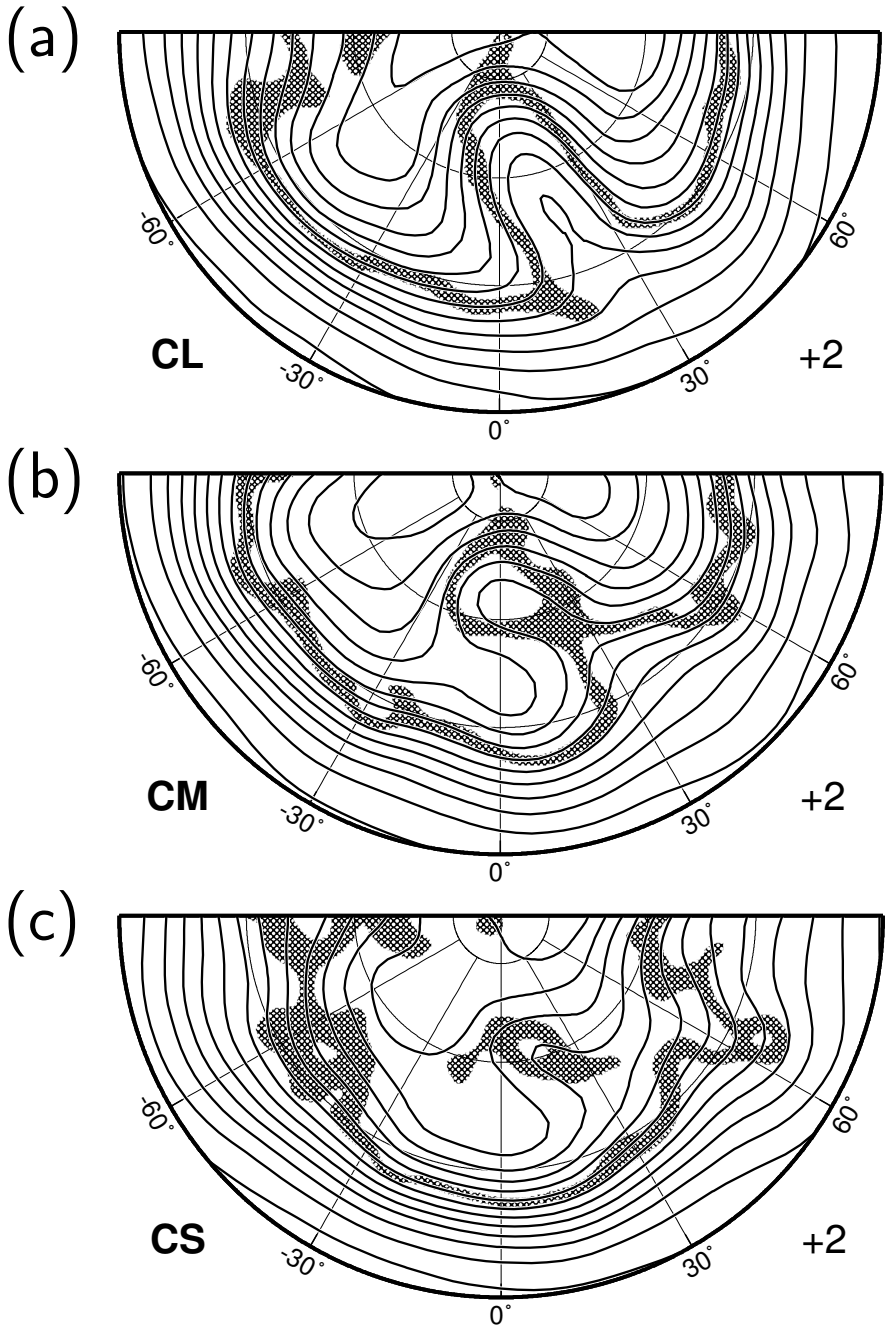

Figure 4.26. Composite maps of geopotential height (solid lines) and the approximated isobaric PV ranged from 3 to 4 PVU (shading) at 250-hPa level at +2 days relative to the onset time for (a) CL, (b) CM and (c) CS. Contour interval is 100 m.

Table 4.3. A list of CS events.

No.	**Onset Time**				**Central Longitude** (deg)	**Duration** (day)	**Mature B-index** (m)	**C-index** (Wm^{-2})
1	12Z	5	March	1983	200.0	7.25	-217.66	0.73
2	00Z	4	February	1984	147.5	7.50	-331.73	0.72
3	12Z	22	January	1985	162.5	7.25	-168.97	0.67
4	00Z	1	January	1983	155.0	7.00	-200.47	0.66
5	00Z	22	January	1995	170.0	12.75	-272.40	0.34
6	12Z	9	January	1975	140.0	10.00	-350.67	0.07
7	18Z	13	March	1965	147.5	10.00	-246.61	0.07
8	12Z	6	March	1987	147.5	7.75	-180.38	0.05
9	06Z	12	December	1999	150.0	9.00	-224.72	-0.07
10	06Z	6	February	1956	147.5	7.25	-251.15	-1.13

4.3.2 Differences between blocking and non-blocking

Recalling the result in Fig. 4.12, it is clear that the low-index event with large C-index does not always become a blocking. The comparison of a blocking and a non-blocking with a large C-index gives a significant information whether or not a transient ridge grows a strong blocking. The non-blocking cases having the 21 largest C-index are then defined as "NB". The NB members is listed in Table 4.4.

Figure 4.27 shows the composite maps of 250-hPa geopotential height, 250-hPa PV, and K_m associated with NB cases. At the onset time, 250-hPa geopotential height and PV fields are similar to the CL composite, and the inversion of meridional PV gradient occurs at 0° longitude. Although the low-PV air intrudes deeply into high latitudes, the ridge moves eastward and becomes narrower. Finally, the low-PV air squashes, the ridge is attenuated, and the flow about 30° longitude becomes more zonally. The maps of K_m show the meandering of jet around 30° longitude at day 0, but the double-jet pattern is not formed, and the flow about 30° longitude weakens afterwards. Unlike CL, K_m around the upstream jet doesn't have the marked enhancement prior to the onset time, and keeps about 4×10^6 Jm^{-2} from day -4 to $+4$.

Figure 4.28 shows the composite maps of the terms in (2.7) and (2.8) for the NB

cases averaged from day −2 to +2. Unlike CL, K_m tends to decrease around the ridge (Fig. 4.28a). $C(K_s, K_m)$ has maxima around the upstream jet and around the ridge, which is similar to CL (Fig. 4.28b). The maximum of $C(K_s, K_m)$ is comparable with CL around the ridge. The distributions of $C_D(K_s, K_m)$ and $C_{ND}(K_s, K_m)$ are also similar to CL around the ridge (Fig. 4.29). It is about a half of CL at the entrance of the upstream jet (about $-60°$ longitude). It is noteworthy that $B(K_m + \Phi_m)$ is negative around the ridge in the opposite sense of CL (Fig. 4.28e). The negative $B(K_m + \Phi_m)$ is due to the negative $B(K_m)$ at this area (Fig. 4.28c). Around the upstream jet, a negative $B(K_m + \Phi_m)$ area is weaker and more eastward than that in CL. The pattern of $B(K_s + \Phi_s) + C(A, K_s)$ is similar to $C(K_s, K_m)$, and $B(K_s + \Phi_s) + C(A, K_s)$ is about twice as large as $C(K_s, K_m)$ (Fig. 4.28f).

Both in CL and in NB, the maximum value of $C(K_s, K_m)$ is located in the upstream jet, and in phase with the maximum of $B(K_s + \Phi_s) + C(A, K_s)$. Although they are similar between the pattern of $B(K_m)$ and $B(K_s)$, and between $G(K_m)$ and $G(K_s)$, $B(K_s + \Phi_s) + C(A, K_s)$ is positive and $B(K_m + \Phi_m)$ is negative around the upstream jet. A positive $B(K_s + \Phi_s) + C(A, K_s)$ in this area is due to a positive $G(K_s)$, which includes $C(A, K_s)$ in part, exceeding a negative $B(K_s)$. Hence, the upstream jet may have strong $C(A, K_s)$. It is indicated that the K_s converted from A is in situ transformed into K_m via $C(K_s, K_m)$ around the upstream jet, which is

just a baroclinic conversion. The same feature appears around the ridge.

Figures 4.30, 4.31 and 4.32 display the time-latitude cross sections of K_m, $C(K_s, K_m)$ and $B(K_m + \Phi_m)$, respectively, for CL, NB and CL−NB averaged from $-30°$ to 45° longitude. While a double-jet pattern is formed in CL, the maximum K_m at 65°N appears at day 0 and decays soon at day 2 in NB (Fig. 4.30). $C(K_s, K_m)$ is the maximum at 65°N in both CL and NB, but the maximum in NB is rather smaller than that in CL after day +2 (Fig. 4.31). The term which is the most different between CL and NB is $B(K_m + \Phi_m)$ as shown in Fig. 4.32. In NB, a positive impact of $B(K_m + \Phi_m)$ around 70°N at day 0 is much smaller than that in CL. Nevertheless, a strong negative of $B(K_m + \Phi_m)$ at this area reduces K_m at day +1.5. This is correspondent to Fig. 4.28(e).

Figure 4.33 shows the time series of the terms in (2.7) averaged in the ridge area ($-30°$ to 45° in longitude, and 50°N to 80°N in latitude) for (a) CL and (b) NB composites. In both composites, positive K_m tendency (dashed line) gradually increases toward the onset and reaches about 4 Wm^{-2} at the onset time. After the onset, K_m tendency decreases in both composites, the NB decreases more rapidly than CL. Since the selected cases have large values of C-index, these two composites are similar in the time series of $C(K_s, K_m)$. However, the time series of $B(K_m + \Phi_m)$ (thick solid line) is different between CL and NB. In CL, $B(K_m + \Phi_m)$ is roughly zero

or positive during the period shown in Fig. 4.33. It is comparable with $C(K_s, K_m)$ at the onset and is about zero after day +2. In NB, on the other hand, it is a half of $C(K_s, K_m)$ at the onset. At day +2, it reaches the maximum value (about -5 Wm^{-2}), which is comparable with $C(K_s, K_m)$ but opposite sign.

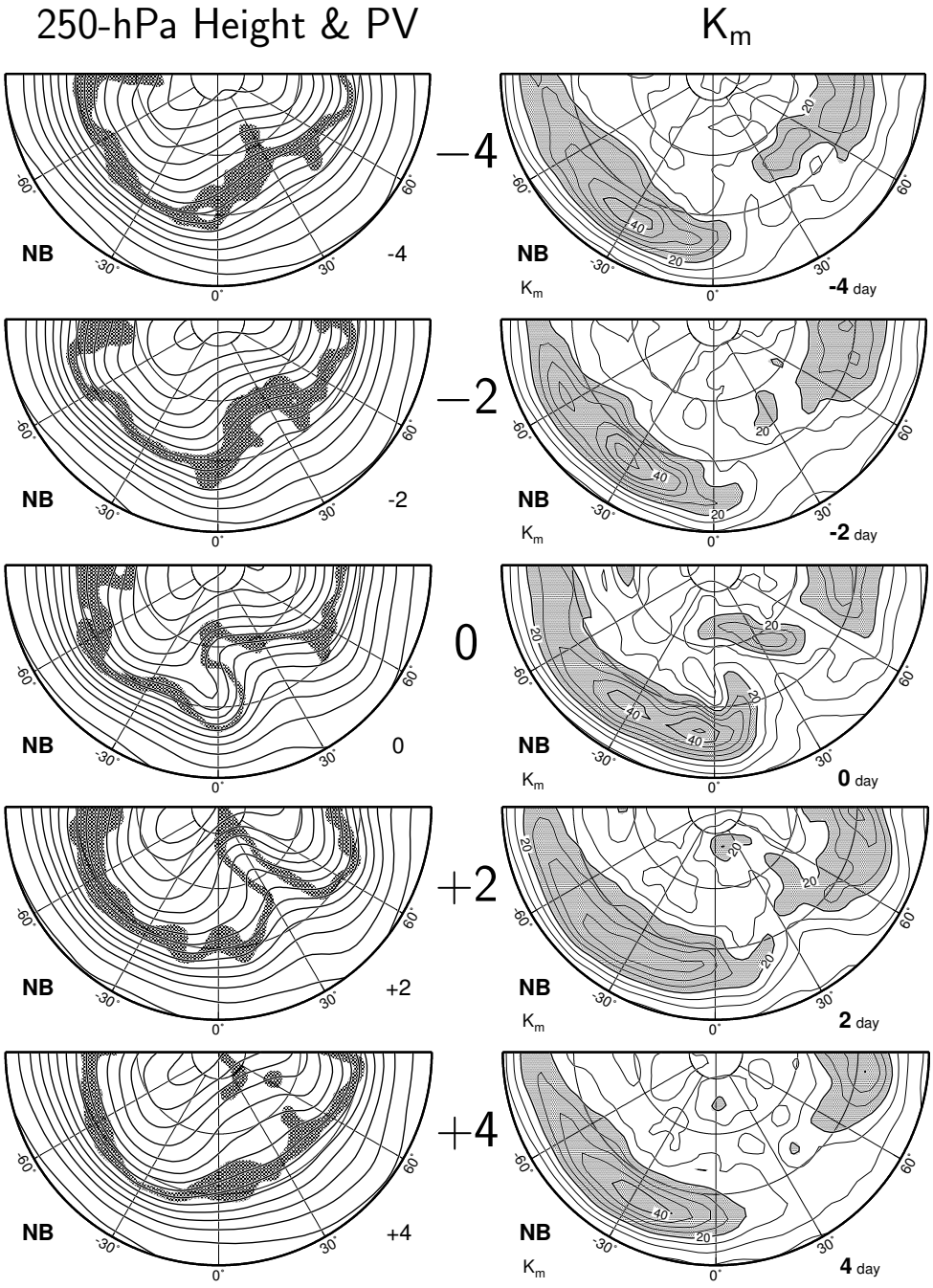

Figure 4.27. As in Fig. 4.14 except for NB composite.

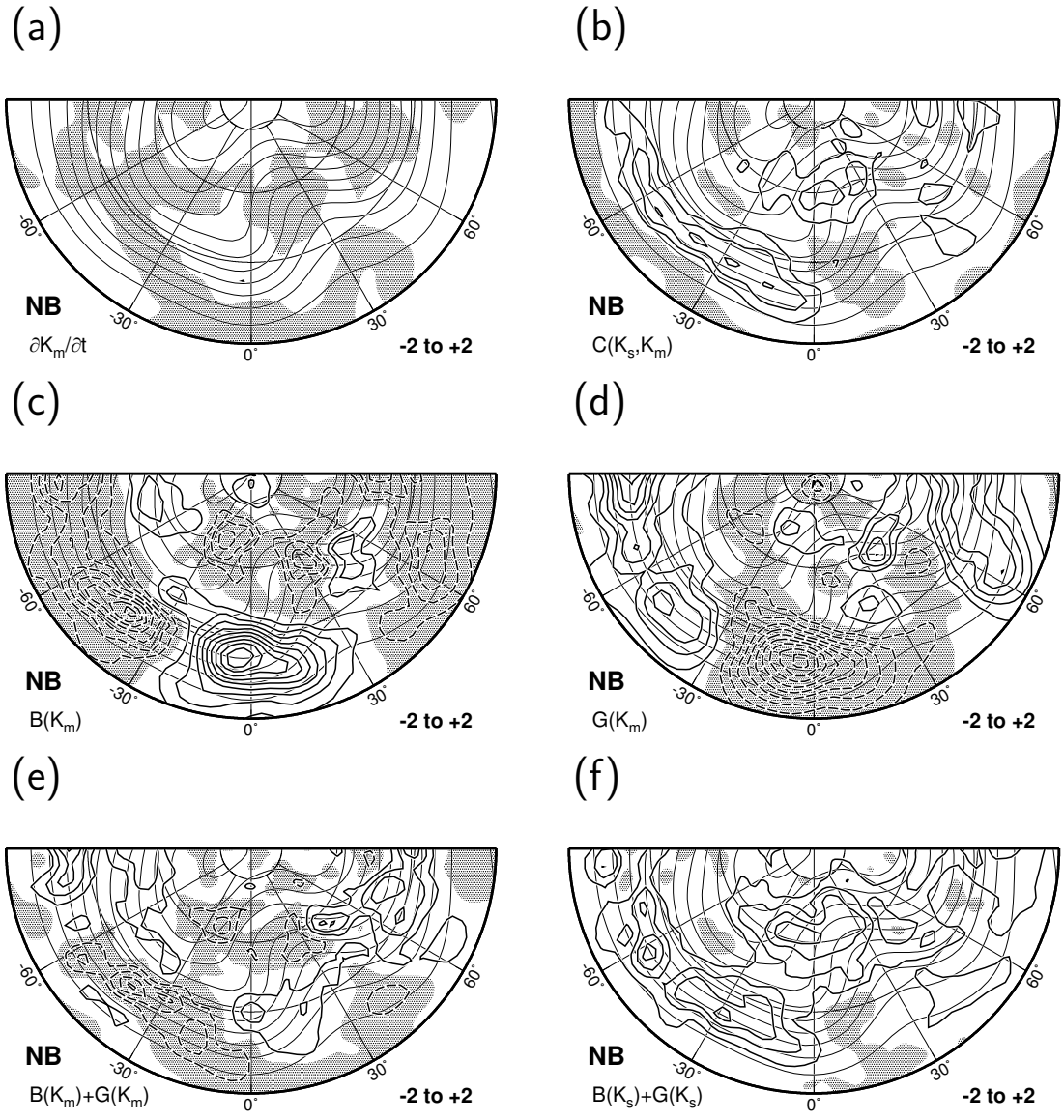

Figure 4.28. As in Fig. 4.17 except for NB composite.

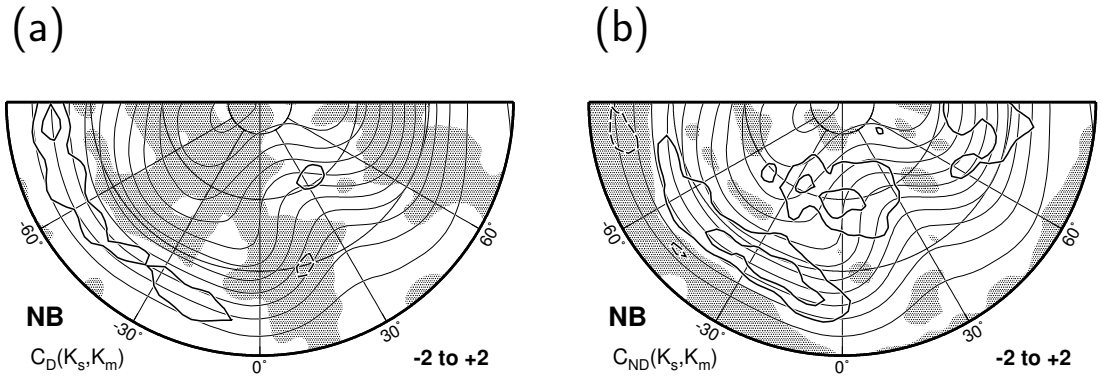

Figure 4.29. As in Fig. 4.20 except for NB composite.

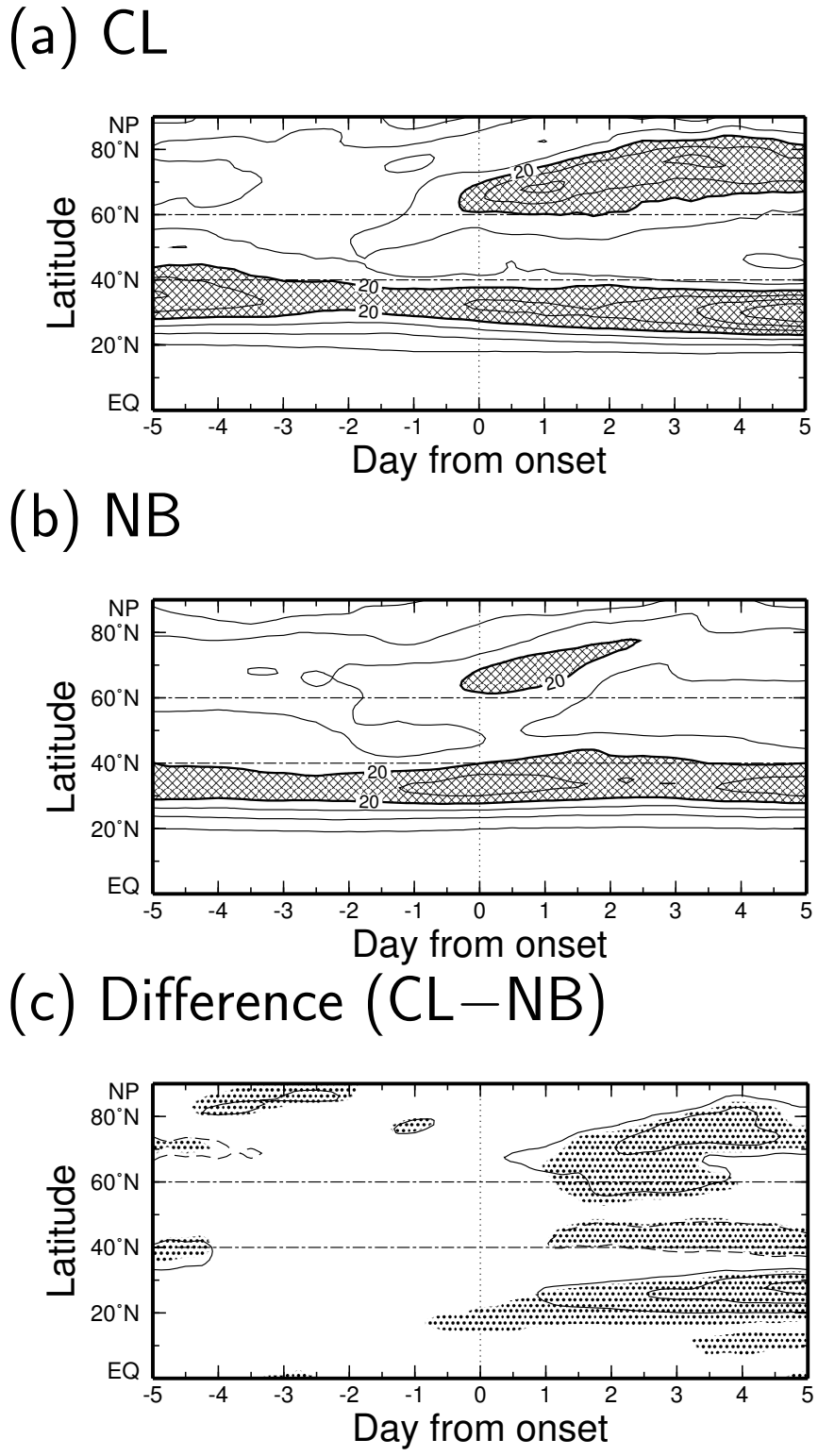

Figure 4.30. As in Fig. 4.23 except for (a) CL, (b) NB and (c) CL−NB.

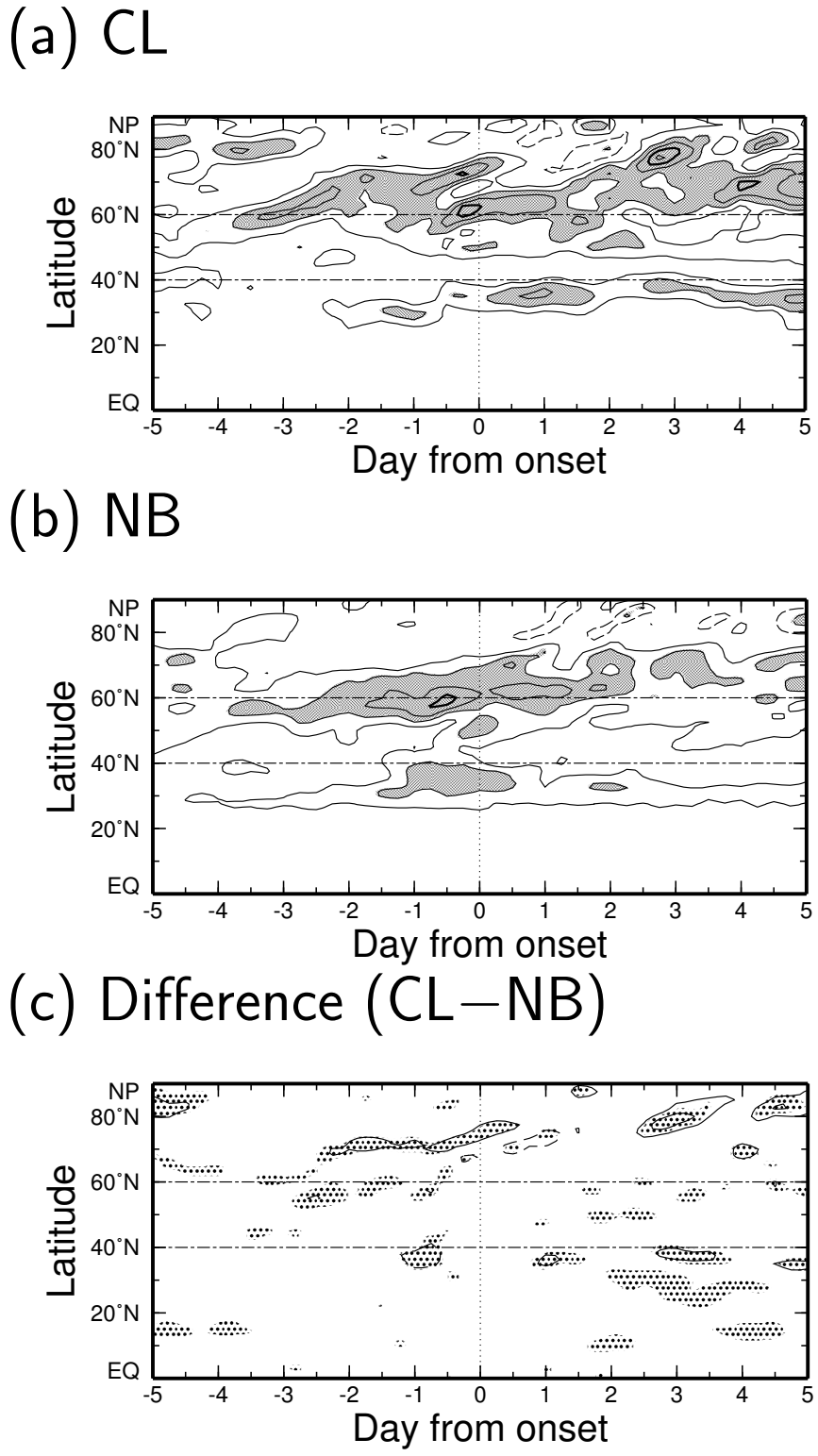

Figure 4.31. As in Fig. 4.24 except for (a) CL, (b) NB and (c) CL−NB.

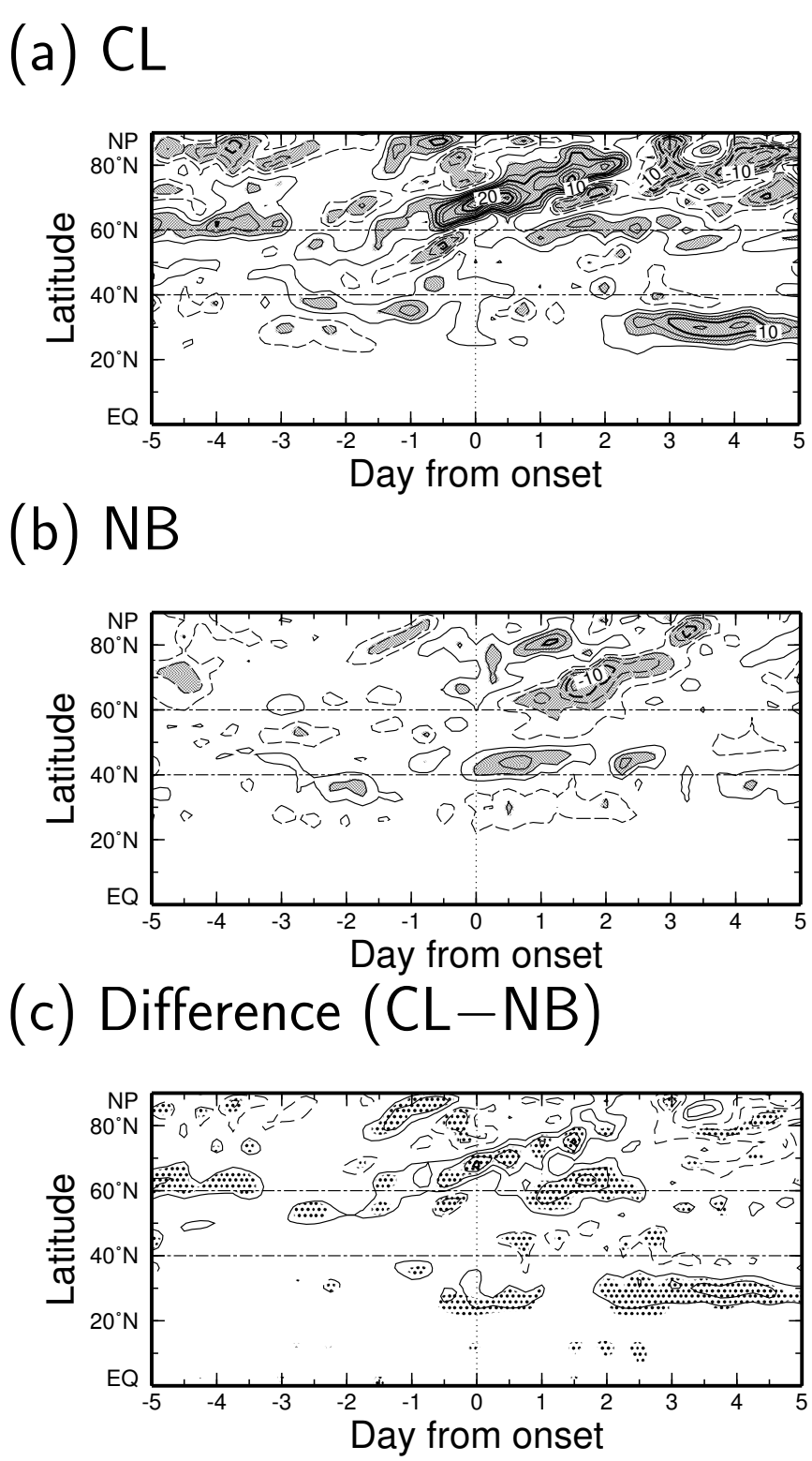

Figure 4.32. As in Fig. 4.25 except for (a) CL, (b) NB and (c) CL−NB.

Table 4.4. A list of NB events.

No.	**Onset Time**				**Central Longitude** (deg)	**Duration** (day)	**Mature B-index** (m)	**C-index** (Wm^{-2})
1	12Z	30	January	2000	227.5	0.25	-96.93	8.28
2	00Z	26	December	1992	167.5	1.25	-53.73	8.10
3	06Z	19	January	1982	180.0	0.50	-110.27	7.79
4	18Z	17	December	1990	195.0	1.50	-193.26	7.39
5	18Z	10	January	1962	177.5	1.00	-110.49	7.36
6	12Z	20	January	1981	217.5	1.25	-219.07	7.32
7	18Z	1	December	1991	190.0	0.50	-87.94	6.43
8	06Z	12	February	1989	197.5	1.75	-180.16	6.36
9	12Z	21	February	1988	185.0	2.00	-130.21	6.23
10	12Z	22	January	1951	165.0	0.25	-67.87	6.09
11	00Z	25	February	1989	220.0	2.25	-229.93	6.07
12	18Z	7	January	1997	192.5	1.75	-148.99	6.02
13	06Z	12	January	1972	175.0	0.25	-79.54	5.75
14	00Z	29	November	1973	162.5	0.25	-69.30	5.74
15	00Z	17	November	1996	207.5	0.25	-98.32	5.72
16	00Z	24	January	2000	222.5	0.25	-65.38	5.35
17	12Z	4	January	1956	170.0	0.25	-49.78	5.33
18	18Z	23	February	1982	165.0	1.25	-200.00	5.32
19	18Z	13	November	1950	177.5	1.00	-106.19	5.24
20	18Z	25	February	1982	150.0	1.25	-108.99	5.17
21	12Z	22	November	1970	207.5	0.75	-144.06	5.04

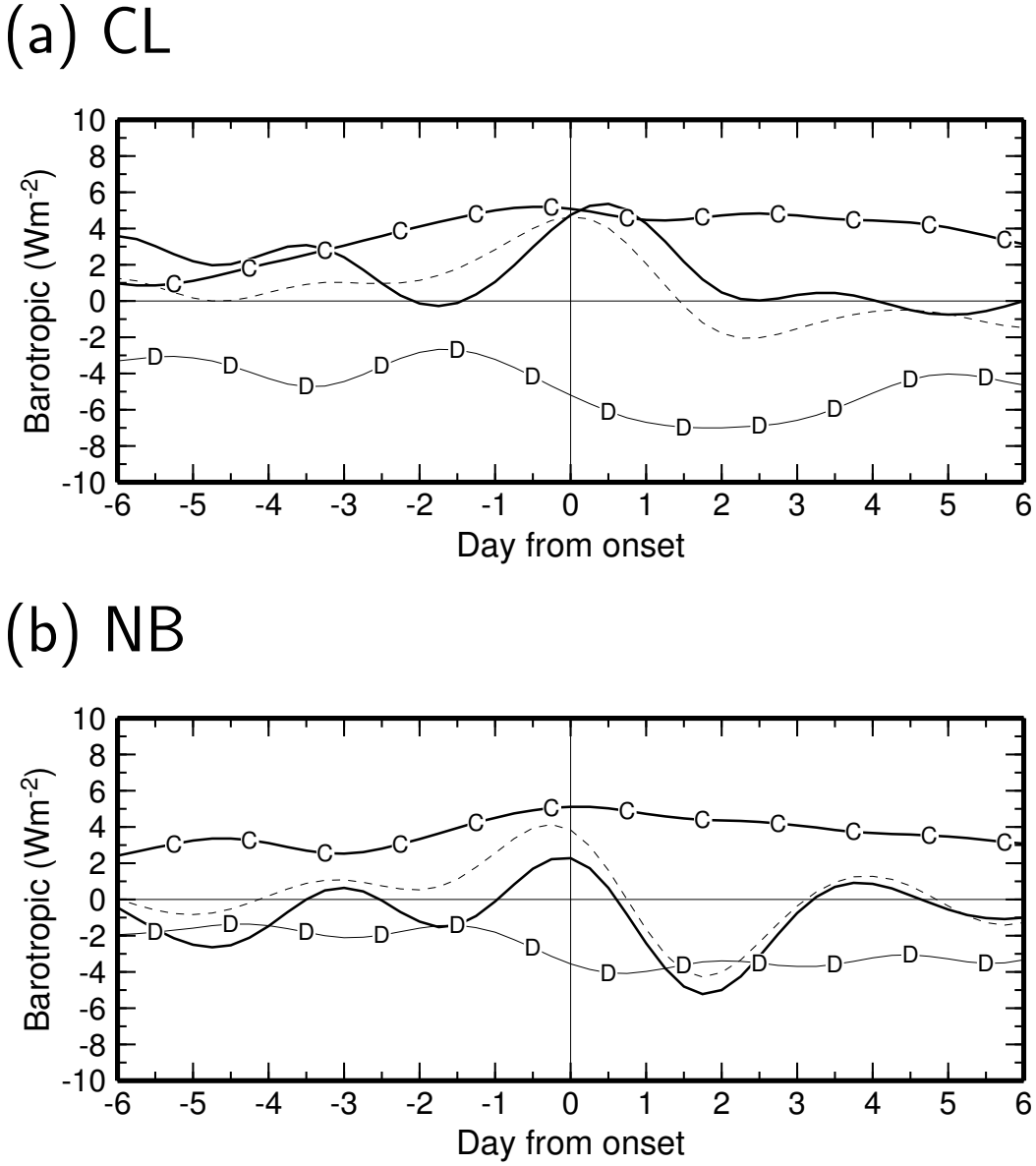

Figure 4.33. Time series of the K_m tendency (dashed line), $B(K_m+\phi_m)$ (thick solid line), $C(K_s, K_m)$ (labeled "C") and the residual dissipation term, $D(K_m)$ (labeled "D") for (a) CL and (b) NB composites. All values are averaged in the ridge area ranged from $-30°$ to $45°$ of longitude, and from 50°N to 80°N of latitude.

CHAPTER V
DISCUSSION

CHAPTER VI
CONCLUSIONS

ACKNOWLEDGMENTS

First of all, I thank Dr. H.L. Tanaka of the University of Tsukuba very much for your pertinent advice and guidance. I am also thankful to Dr. F. Kimura and Dr. H. Ueda of the University of Tsukuba, and Dr. T. Yasunari of the Nagoya University for a variety of valuable comments and suggestions. I am most grateful to Mr. M.E. Hori and Mr. D. Nohara of the University of Tsukuba for counseling me on various problems as well as helpful advice on my study. Several comments from Dr. A. Hasegawa of the University of Tokyo, Mr. M. Hayasaki and Dr. Y. Terao of the National Institute for Environmental Studies, and Dr. M. Abe of the Nagoya University were helpful to me.

I am grateful to Mr. M. Hara, Mr. O. Okamura and all other students and staffs of the Climatology and Meteorology Group, the University of Tsukuba, for their comments and supports. I thank Dr. M. Ichise, Mr. A. Ikeda and all other collegues and friends for their encouragement. Finally, I am most thankful my parents and sister for their support and understanding.

Almost all figures are drawn by the Generic Mapping Tools (GMT) graphics (Wessel and Smith 1991).

REFERENCES

Alberta, T. L., S. J. Colucci and J. C. Davenport, 1991: Rapid 500-mb cyclogenesis and anticyclogenesis. *Mon. Wea. Rev.*, **119**, 1186–1204.

Alpert, J. C., 1981: An analysis of the kinetic energy budget for two extratropical cyclones: The vertically averaged flow and the vertical shear flow. *Mon. Wea. Rev.*, **109**, 1219–1232.

Berggren, R., B. Bolin and C. G. Rossby, 1949: An aerological study of zonal motion, its perturbations and break-down. *Tellus*, **1**, 14–37.

Blackmon, M. L., S. L. Mullen and G. T. Bates, 1986: The climatology of blocking events in a perpetual January simulation of a spectral general circulation model. *J. Atmos. Sci.*, **43**, 1379–1405.

Chen, T. C. and Y. H. Lee, 1983: A study of the kinetic energy generation with general circulation models. *J. Meteor. Soc. Japan*, **61**, 439–448.

Chen, T. C. and M. C. Yen, 1985: A note on the kinetic energy budget analysis of the atmospheric baroclinic and barotropic flows. *J. Meteor. Soc. Japan*, **63**, 685–693.

Colucci, S. J., 1985: Explosive cyclogenesis and large-scale circulation changes: Implications for atmospheric blocking. *J. Atmos. Sci.*, **42**, 2701–2717.

Dole, R. M. and N. D. Gordon, 1983: Persistent anomalies of the extratropical northern hemisphere wintertime circulation: Geographical distribution and regional persistence characteristics. *Mon. Wea. Rev.*, **111**, 1567–1586.

Green, J. S. A., 1977: The weather during July 1976: Some dynamical considerations of the drought. *Weather*, **32**, 120–126.

Haines, K. and J. Marshall, 1987: Eddy-forced coherent structures as a prototype of atmospheric blocking. *Quart. J. R. Met. Soc.*, **113**, 681–704.

Hansen, A. R. and A. Sutera, 1984: A comparison of the spectral energy and enstrophy budgets of blocking versus nonblocking periods. *Tellus*, **36A**, 52–63.

Kalnay, E., M. Kanamitsu, R. Kistler, W. Collins, D. Deaven, L. Gandin, M. Iredell, S. Saha, G. White, J. Woollen, Y. Zhu, M. Chelliah, W. Ebisuzaki, W. Higgins, J. Janowiak, K. C. Mo, C. Ropelewski, J. Wang, A. Leetmaa, R. Reynolds, R. Jenne and D. Joseph, 1996: The NCEP/NCAR 40-year reanalysis project. *Bull. Amer. Meteor. Soc.*, **77**, 437–471.

Kasahara, A. and K. Puri, 1981: Spectral representation of three-dimensional global data by expansion in normal mode functions. *Mon. Wea. Rev.*, **109**, 37–51.

Lejenäs, H. and H. Økland, 1983: Characteristics of northern hemisphere blocking as determined from a long time series of observational data. *Tellus*, **35A**, 350–362.

Lupo, A. R., 1997: A diagnosis of two blocking events that occurred simultaneously in the midlatitude northern hemisphere. *Mon. Wea. Rev.*, **125**, 1801–1823.

Lupo, A. R. and P. J. Smith, 1994: Climatological features of blocking anticyclones in the northern hemisphere. *Tellus*, **47A**, 439–456.

Lupo, A. R. and P. J. Smith, 1998: The interactions between a midlatitude blocking anticyclone and synoptic-scale cyclones that occurred during the summer season. *Mon. Wea. Rev.*, **126**, 502–515.

Mak, M., 1991: Dynamics of an atmospheric blocking as deduced from its local energetics. *Quart. J. R. Met. Soc.*, **117**, 477–493.

Marques, R. F. C. and V. B. Rao, 1999: A diagnosis of a long-lasting blocking event over the southeast Pacific ocean. *Mon. Wea. Rev.*, **127**, 1761–1776.

Mullen, S. L., 1986: The local balances of vorticity and heat for blocking anticyclones in a spectral general circulation model. *J. Atmos. Sci.*, **43**, 1406–1441.

Mullen, S. L., 1987: Transient eddy forcing of blocking flows. *J. Atmos. Sci.*, **44**, 3–22.

Nakamura, H. and J. M. Wallace, 1990: Observed changes in baroclinic wave activity during the life cycles of low-frequency circulation anomalies. *J. Atmos. Sci.*, **47**, 1100–1116.

Nakamura, H. and J. M. Wallace, 1993: Synoptic behavior of baroclinic eddies during the blocking onset. *Mon. Wea. Rev.*, **121**, 1892–1903.

Nakamura, H., M. Nakamura and J. L. Anderson, 1997: The role of high- and low-frequency dynamics in blocking formation. *Mon. Wea. Rev.*, **125**, 2074–2093.

Rex, D. F., 1950a: Blocking action in the middle troposphere and its effect upon regional climate I. an aerological study of blocking action. *Tellus*, **2**, 196–211.

Rex, D. F., 1950b: Blocking action in the middle troposphere and its effect upon regional climate. II. The climatology of blocking action. *Tellus*, **2**, 275–301.

Sheu, Y. T. P. and P. J. Smith, 1981: A kinetic climatology of flow regimes associated with 500 mb waves over North America in winter and spring. *Mon. Wea. Rev.*, **109**, 1862–1878.

Shutts, G. J., 1983: The propagation of eddies in diffluent jetstreams: eddy vorticity forcing of 'blocking' flow fields. *Quart. J. R. Met. Soc.*, **109**, 737–761.

Simmons, A. J. and B. J. Hoskins, 1978: The life cycles of some nonlinear baroclinic waves. *J. Atmos. Sci.*, **35**, 414–432.

Smagorinsky, J., 1963: General circulation experiments with the primitive equations. I: The basic experiment. *Mon. Wea. Rev.*, **91**, 99–165, out of possession.

Tanaka, H., 1985: Global energetics analysis by expansion into three-dimensional normal mode functions during the FGGE winter. *J. Meteor. Soc. Japan*, **63**, 180–200.

Tanaka, H. L., 1991: A numerical simulation of amplification of low-frequency planetary waves and blocking formations by the upscale energy cascade. *Mon. Wea. Rev.*, **119**, 2919–2935.

Tanaka, H. L., 1998: Numerical simulation of a life-cycle of atmospheric blocking and the analysis of potential vorticity using a simple barotropic model. *J. Meteor. Soc. Japan*, **76**, 983–1008.

Tanaka, H. L. and E. C. Kung, 1988: Normal mode energetics of the general circulation during the FGGE year. *J. Atmos. Sci.*, **45**, 3723–3736.

Tibaldi, S. and F. Molteni, 1990: On the operational predictability of blocking. *Tellus*, **42A**, 343–365.

Treidl, R. A., E. C. Birch and P. Sajecki, 1981: Blocking action in the northern hemisphere: a climatological study. *Atom.-Ocean*, **19**, 1–23.

Watarai, Y., 2000: The role of barotropic-baroclinic interactions for the formation and the maintenance of blocking. Master's thesis, Graduate School of Geoscience, University of Tsukuba, 63 pp. (in Japanese with English abstract).

Wessel, P. and W. H. F. Smith, 1991: Free software helps map and display data. *EOS Trans. Amer. Geophys. U.*, **72**, 445–446.

Wiin-Nielsen, A., 1962: On transformation of kinetic energy between the vertical shear flow and the vertical mean flow in the atmosphere. *Mon. Wea. Rev.*, **90**, 311–323.

Wiin-Nielsen, A., 1967: On the annual variation and spectral distribution of atmospheric energy. *Tellus*, **19**, 540–559.

Wiin-Nielsen, A. and M. Drake, 1965: On the energy exchange between the baroclinic and barotropic components of atmospheric flow. *Mon. Wea. Rev.*, **93**, 79–92.